3D printing lightweight mortars with cork to improve thermal efficiency in buildings

Please check the document version of this publication:

• A submitted manuscript is the version of the article upon submission and before peer-review. There can be important differences between the submitted version and the official published version of record. People interested in the research are advised to contact the author for the final version of the publication, or visit the DOI to the publisher's website.
• The final author version and the galley proof are versions of the publication after peer review.
• The final published version features the final layout of the paper including the volume, issue and page numbers.

Link to publication

3D printing lightweight mortars with cork to improve thermal efficiency in buildings

C.M. Rangel [a,*], A.S. Guimarães [b], T.A.M. Salet [a], S.S. Lucas [a]

[a] *Department of the Built Environment, Eindhoven University of Technology, De Zaale, Eindhoven 5612 AZ, the Netherlands*
[b] *CONSTRUCT-LFC, Faculty of Engineering (FEUP), University of Porto, Rua Dr. Roberto Frias, Porto 4200-465, Portugal*

ARTICLE INFO

ABSTRACT

3D printing lightweight aggregate concrete potentially allows building components with reduced thickness and lighter structures. However, the effect of lightweight additives in 3D printing compositions, particularly the use of cork, in the fresh and hardened properties of 3DP is still unknown. This study demonstrates that adding increasing amounts of cork (0%, 25%, 50%, 75%, and 100%) in place of fine sand enhances the insulation of printable mortars. Cork mortars positively reduced the required yield stress at the bottom layer in the fresh state due to lighter bulk densities. Attaining lower hardened densities (1363.0–1791.5 Kg/m^3), printed mortars with high amounts of cork (50, 67, and 100%) showed fair values of thermal conductivity ranging between 0.40 and 0.96 W/mk, for a value of 1.42 W/mk of the reference. Cork composites presented sufficient mechanical strength, with a compressive strength between 21.1 MPa at 100% cork and 51.1 MPa at 17% cork compared to 58.3 MPa of reference mortar. Printing did not considerably affect strength development or thermal conductivity in printed mortars. The latest showed isotropic behavior in all test directions, while mild anisotropy was found for compressive and tensile strength. Micro and macrostructure analysis revealed that printing reduces macropores in the sample's core relative to the compaction of lightweight aggregate mortars. When applied on a large scale, these composites can bring printed constructions closer to meeting thermal comfort standards with reduced self-weight.

1. Introduction

The global building sector consumes approximately 30% of global energy (135 EJ) and is responsible for about 27% of global operational-related CO_2 emissions (10 GtCO2) [1]. The production of important materials used in construction, concrete, steel, and aluminum added a further 4% of global energy use and 6% of global emissions in 2021[1]. It is alarming that to be aligned with reaching net zero carbon emissions by 2050, global emissions would need to fall by over 98 percent from 2020 levels [2]. Thus, engineering energy-efficient buildings must be a priority to meet the Paris Agreement by 2030 and 2050.

In energy-efficient buildings, materials must theoretically balance heat conductivity and mechanical properties. Despite research efforts to produce thermally resistant systems to reduce energy consumption, few building materials can provide suitable insulation while minimizing geometric building envelope sizes. Lightweight aggregate concrete (LWAC) is an example of a material that offers a combination of strength and insulating properties by partially or entirely replacing normal-

weight aggregate (i.e., sand and gravel) with lightweight aggregate (LWA) [3]. While this type of concrete was previously used to make fair-faced walls and slabs in the past, due to stricter building codes, cast monolithic external walls made of LWAC with an economical thickness are no longer acceptable [4].

Unlike casting, 3D printing (3DP) concrete allows printed elements with various and optimized geometries due to the absence of formwork [5]. By coordinating computer-aided design, the printing system (i.e., pump and printer), and the material properties, designers have created building components with reduced thickness and potentially lighter structures [6]. Few researchers have investigated whether the 3D-printed building can be better prepared to meet thermal comfort standards [7]. For instance, a few works proposed benefiting from the shape of the print path to stimulate a thermal lag through the printed element [8–10]. However, developing a suitable material that combines strength and insulating properties is crucial to its success.

Researchers have looked at the effect of lightweight additives like expanded perlite [11], expanded glass [12], and tire rubber waste [13,

---

* Corresponding author.
E-mail address: c.maciel.rangel@tue.nl (C.M. Rangel).

14] on LWA 3DP concrete [7]. However, no study has looked in detail at how cork affects the fresh and hardened properties of 3DP. Regarding sustainable development, cork is a promising alternative to commonly used sintered lightweight aggregates produced by intense heat treatment of natural sources, such as clay, shale, or slate. Firstly, cork demonstrates a significantly lower environmental impact than materials generated via a sintering process since it is extracted from the outer layer of cork oak trees (*Quercus suber*) without causing harm to the trees themselves. Studies indicate that cork oak forests capture 73 tons of CO_2 annually for each ton of cork produced, contributing to the prevention of global warming [15]. Roughly 25% of harvested cork is employed in creating high-quality punched bottle stoppers, while the remaining 75% is transformed into granules of varying sizes. These cork remnants can be repurposed to fabricate composites like insulation boards [16]. Secondly, the exceptional hygrothermal and mechanical properties of granulated cork, coupled with its low density (0.120 g/cm³) and remarkable dimensional stability [17], make it a good filler and lightweight aggregate in concrete [18], mortars, and rendering [19–22]. Its incorporation substantially enhances the thermal and physical attributes of the resulting composites.

With limited delve into the material's properties, a few studies attempted to demonstrate how modifying the 3DC printing system enables the creation of a functionally graded material [23,24], as in the example of cork as LWA. Proper knowledge of the material design, how the use of cork can benefit the printability of mortars, and the advantages in thermal-physical behavior have yet to be developed.

In the current study, we investigate the influence of virgin granulated cork of 0.5–2 mm on the fresh and hardened properties of 3D printable concrete to give a practical alternative to lower the self-weight and improve the thermal resistance of 3DCP elements. The fresh properties, such as consistency in use, fresh density, and spread flow, are obtained to fine-tune the printing parameters (i.e., printing speed and extrusion rate). Furthermore, this work analyses how increasing cork content positively affects the printing parameters, such as printing speed and mortar buildup. Printing is carried in an articulated robot using a constant displacement extruder. To assess the hardened properties, samples were extracted from printed elements and then subjected to compression, flexural, and tensile tests and thermal conductivity measurements in different loading directions. Finally, the influence of natural and lightweight aggregate on macro and microstructure, mechanical, and thermo-physical properties are examined. When applied on a large scale, these composites can bring printed constructions closer to meeting thermal comfort standards with reduced self-weight.

In this study, we look at how 0.5–2 mm of virgin granulated cork affects the fresh and hardened properties of 3D printable concrete. The goal is to find a practical way to lower the self-weight of 3DCP elements and improve their thermal resistance. The fresh properties, such as consistency in use, fresh density, and spread flow, are obtained to fine-tune the printing parameters (i.e., printing speed and extrusion rate). Furthermore, this work analyzes how increasing cork content positively affects printing parameters such as printing speed and mortar buildup. Printing is carried out by a 6-axis robot arm moving along axes X, Y, and Z that supports a constant displacement extruder. To assess the hardened properties, samples were extracted from printed elements and then subjected to compression, flexural, and tensile tests and thermal conductivity measurements in different loading directions. Finally, the influence of natural and lightweight aggregates on macro and microstructure, mechanical, and thermo-physical properties is examined. When applied on a large scale, these composites can bring printed constructions closer to meeting thermal comfort standards with reduced self-weight.

2. Materials and methods

2.1. Materials

Cork presents remarkable hygrothermal properties stemming from a combination of its microstructure and chemical composition [25]. Its structure is composed of microcells, typically with a length of 40 µm, that resembles a tetrakaidecahedron connected by capillaries, as seen in Fig. 1. These microcells (Fig. 1(b,d)) have 90% of their volume filled with gas, giving cork its low specific weight, within the range of 190–250 kg/m³ [26]. As a result of both the gas content and cell size, cork has inferior heat transfer properties with a low thermal conductivity coefficient (λ-value) of 0.037–0.040 W/mK. Cork's main chemical components are suberin (33–62 wt%), lignin (13–27 wt%), cellulose and polysaccharides (6–26 wt%), and in smaller fractions, extractable substances (e.g., tannin, glycerine) and mineral components (e.g., potassium, sodium) [25]. The concentration of each constituent may vary depending on the geographical extraction, the morphological location of the tree, the age, and the climate conditions.

To reduce the mortar's density, virgin cork granules (CG) of 0.120 g/cm³ specific particle density, as provided by the manufacturer, obtained by grinding cork boards of bottle stoppers production into 0.5–2 mm (Fig. 2) size, were used to gradually replace fine sand of a specific density of 2.65 g/cm³. The quartz sand has a specific grain size distribution ranging between 0.08 and 2 mm, with a maximum moisture content of 0.2%, according to EN 196–1 [27].

In addition to using a more sustainable aggregate, this work employs low-clinker cement (CEM IIIB N LH/SR 42.5 N) in mortars to mitigate the carbon footprint associated with cement production. The slag cement made with 29 wt% average clinker content, 68 wt% of slag, and the remaining 3 wt% of minor compounds has a specific surface of 4500 cm³/g according to EN196–6 [28], a 10 µm mean particle size obtained with a Mastersizer Analyzer, a 2.81 g/cm³ specific density measured in the gas displacement pycnometer Accupyc-II-1345, and a characteristic cubic compressive strength of 42.5 MPa at 28 days. The particle size distribution of raw materials employed in the mix design can be seen in Fig. 3, while Table 1 describes the chemical composition of slag cement under EN 196–2 [29]. A high-range water reducer polycarboxylate ether (PCE)-based with 35% solid content and a specific 1.07 g/cm3 density was employed to lower mortars' water demand. Generally referred to as superplasticizer, this chemical admixture improves the mortar's consistency by reducing the yield stress, which is the energy required to break down a network of interparticle interaction bonded by attractive Van der Waals and colloidal forces whose strength depends on the cement particle's distance. These interparticle forces become repulsive in the superplasticizer's presence, decreasing the cement suspension's yield stress [30] and the water demand to achieve similar consistencies.

2.2. Experimental procedures

2.2.1. Mixing design and mixing procedure

This experimental campaign adopted a mix proportion to gradually reduce the mortar's density, maintaining a fixed aggregate-to-binder ratio of 1.6 by volume. To achieve lower densities, cork granules of particle sizes 0.5–1 mm (CG1) to 1–2 mm (CG2) replaced sand at 0, 25%, 50%,75%, and 100% by volume. The fine sand fraction (0.08–0.5 mm), which made up 33% of the total sand in the reference mortar, was kept the same in these mixes because it is known that fines help form a lubrication layer during the extrusion process [31,32]. Mixtures are called CR, an acronym for cork, followed by their percentage in the total aggregate volume. To further compare a mix with only sand and another with only cork, an additional mix, CR100, has been added to the set, in which CG1 also replaced the fine sand fraction, making up the total aggregate volume.

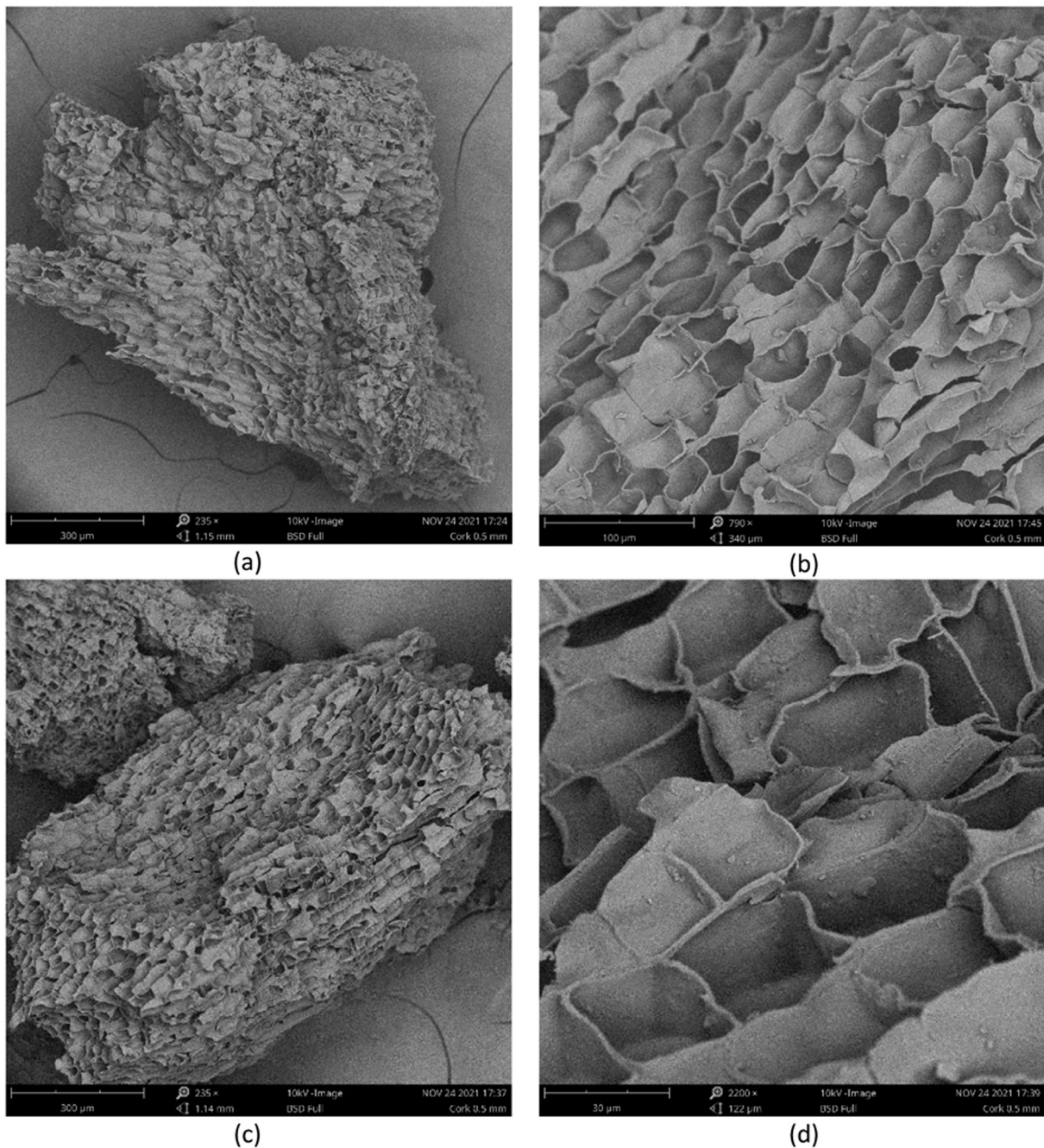Like many other lightweight aggregates (LWA), cork possesses a

Fig. 1. (a) SEM image of a 0.5 mm cork granule shows the cork's rough surface composed of open cells from the grinding process and remaining closed cells; (b) Detailed tetrakaidecahedron structure of cork surface at a higher magnitude. The cell's length is typically 40 μm. (c) The elongated shape of a cork granule contrasts with an angular shape at (a). (d) Magnification of damaged cork cells due to the grinding process.

porous structure consisting of interconnected and enclosed cells. This microstructure enables a certain degree of water infiltration into these cells, consequently raising the water requirement within the fresh cementitious mixture. Thus, it is crucial to consider the amount of water uptake by a LWA in the mix design. The total mix of water (w_t) is then computed as the sum of water for the cement hydration (w_{eff}) and the water absorption of cork (wa). A water-to-cement ratio (w_t/c) of 0.36 was selected to provide mixes with enough workability and sufficient strength. A high-generation water reducer was employed to achieve similar consistency among mixtures with varying cork content. Table 2 shows the quantities of raw materials per cubic meter of concrete.

A planetary mixer set at 50 Hz and 76 rpm mixing frequency was used to make the mortars. The mixing procedure consisted of preparing the cement paste with sand while the cork was partially saturated with water equivalent to 5 minutes (wa_5) absorption in a separate mixer. Water with diluted superplasticizer was continuously added to the cement to prepare the paste for one minute. The slurry was further mixed for 3 minutes, as required for the superplasticizer to act. After that, sand was incorporated into the slurry and mixed for two more minutes. The total mixing time to prepare the sand mortar was five minutes. The partially saturated cork was then gradually incorporated into the bulk for 2 minutes, resulting in a total mixing time of seven minutes. The inclusion of pre-saturated cork, which has been treated with wa_5, is preferred over introducing extra water for saturation (wa) directly into the cement paste and dry cork. This approach has been observed to offer optimal mix stability and prevent the issue of segre-
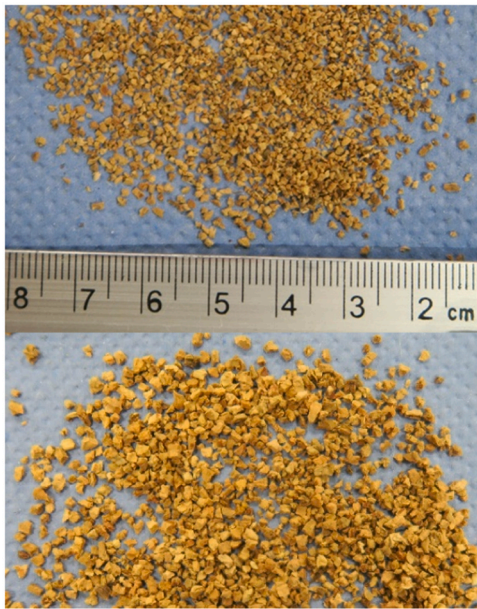
Fig. 2. Morphology of cork granules of 0.5–1 mm (above) and 1–2 mm (below).

gation.

2.2.2. Characterization of physical properties of cork granules

Apparent particle density (ρ_a), oven-dry particle density (ρ_{Lrd}), saturated and surface dry particle density (ρ_{Lssd}), and water absorption at different measuring times $WA_{L(t)}$ were determined following EN 1097–6 Annex C [33]. Two representative samples of 500 ml of CG1 and CG2 were tested. Water absorption was computed as the difference between the mass of a saturated surface-dry (m_{SSD}) specimen in grams after 24 h immersion and its mass in the oven-dry state (m_{OD}) over the oven-dry mass for immersion periods. Intermediate absorption times of 5 min and 1 h were back-calculated from WA_{24h}. In addition to the prescribed procedure, the tea bag infuser method [34] was employed to monitor the mass increase in a continuous immersion of 11 ml of cork granules in water over 24 hours. The test setup is represented in Fig. 4. Three samples of each particle size were tested, and the evolution of water absorption was tracked.

The porosity (P) was determined as the difference between the total volume of the LWA particle and the fractional part of the LWA occupied by solids, computed as the ratio of the relative dry density ρ_{Lrd} and the relative dry density of the solid part ρ_a. Loose bulk density (ρ_b), and voids (n) were obtained by following the procedure described in EN 1097–3:1998 [35] using two samples of each granule size.

2.2.3. Spread flow and bulk fresh density

Both consistency and fresh bulk density are key features in defining the printer parameters, such as the mass flow required to adjust the printing and extrusion speeds. The slump flow table test measured mortar consistency, with the flow table and mold complying with EN

Table 1
Chemical composition of slag cement (CEM IIIB N LH/SR 42.5 N) according to the manufacturer.

Chemical Component	wt%
CaO	44
SiO_2	28
Al_2O_3	11
Fe_2O_3	1
Sulfate SO_3	2.8
Insoluble residue	2.9
Loss on ignition	1.47
Chlorides	0.08
Chromium (VI)*	<0.0002
Na2O equivalent	0.77

Table 2
Mix proportion by kg/m^3 of concrete.

|	REF	CR17	CR34	CR51	CR67	CR100
Vol. fraction cork (φ) [v/v]	0	0.07	0.15	0.22	0.30	0.44
CEM IIIB N LH/SR 42.5 N	772.2	772.2	772.2	772.2	772.2	772.2
Fine sand	376.0	376.0	376.0	376.0	376.0	0.0
Sand 0.5–1 mm	363.3	272.5	181.7	90.8	0.0	0.0
Sand 1–2 mm	418.9	314.2	209.5	104.7	0.0	0.0
Cork 0.5–1 mm	0.0	4.2	8.4	12.6	16.8	34.3
Cork 1–2 mm	0.0	4.8	9.6	14.3	19.1	19.1
Water (w_{eff})	280.4	262.4	244.5	226.5	208.5	173.7
Water absorption of cork 5 min. (wa_5)	0.0	18.0	36.0	53.9	71.9	106.7
Superplasticizer	0.8	0.8	0.8	0.9	0.9	0.9
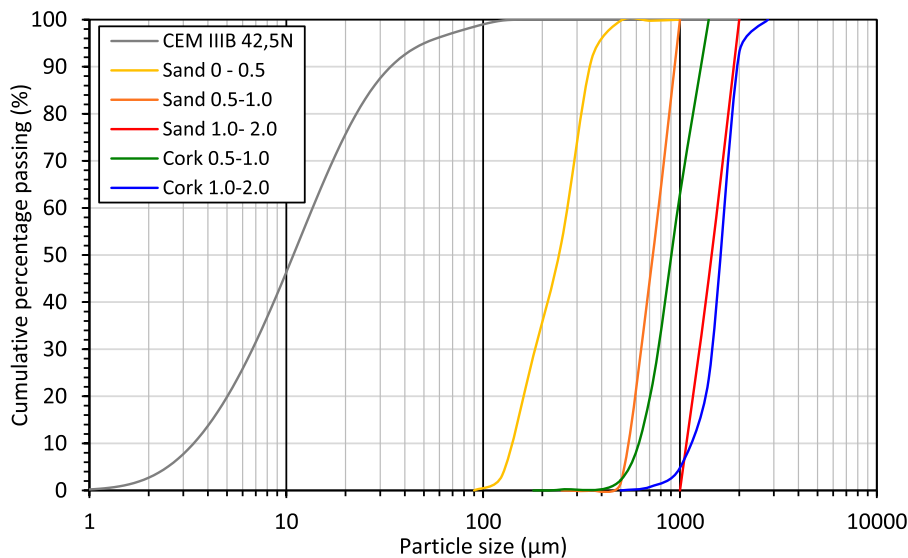
Fig. 3. Particle size distribution of raw material employed in the mix design.
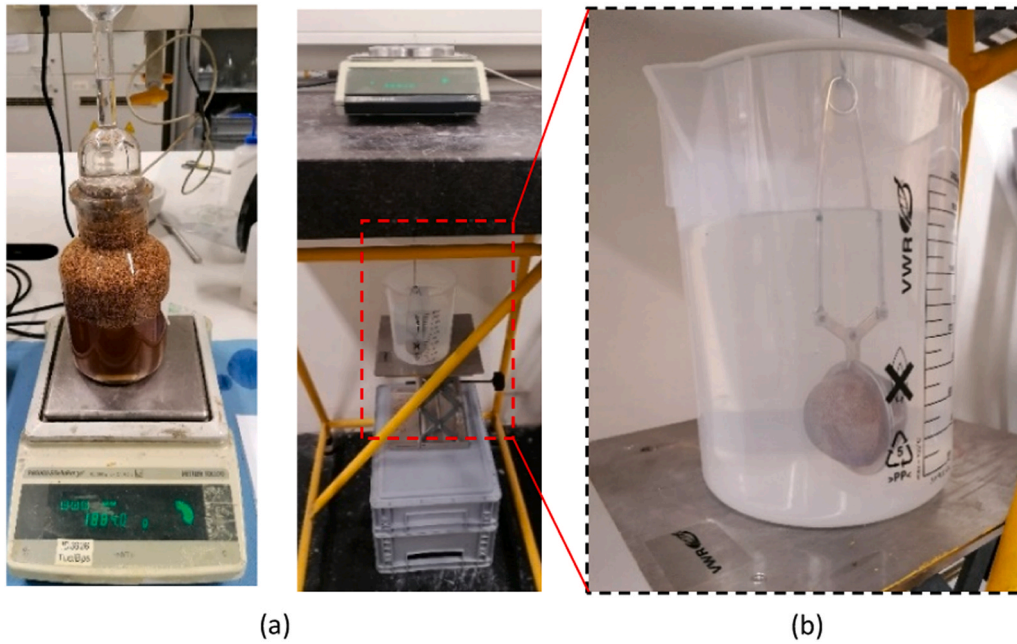
Fig. 4. (a) Water pycnometer test setup used for measurement of water absorption of cork granules. (b)Tea-infuser test setup employed to continuously monitor mass increase in cork granules over 24 h immersion in water.

1015–3 [36]. The slump flow value is computed as the mean of two perpendicular diameter measurements as the material spreads after 15 strikes in the flow table, see Fig. 5(a). The spread flow was monitored every 5 minutes until 15 minutes and then every 15 minutes until 60 minutes to evaluate how cork's water absorption capacity influences the mortar's consistency over time. Before each measurement, the mortar was mixed for 15 seconds at 50 Hz to counteract any false setting that might have occurred. The time zero corresponds to the end of mixing time, which occurs 4–6 minutes after water contacts the cement, marking the start of cement hydration. The change in the flow behavior of mortars containing cork is then compared to the reference mortar that serves as a benchmark.

The density of the fresh mortar was measured by filling a cylindrical stainless vessel with 1 liter of bulk mortar that had been compacted according to the consistency values from the flow table test, as described in EN 1015–6 [37]. Two replicas of each mix design were weighted, and the mean fresh bulk density was derived from the measured mass over the fixed volume (Fig. 5(b)).
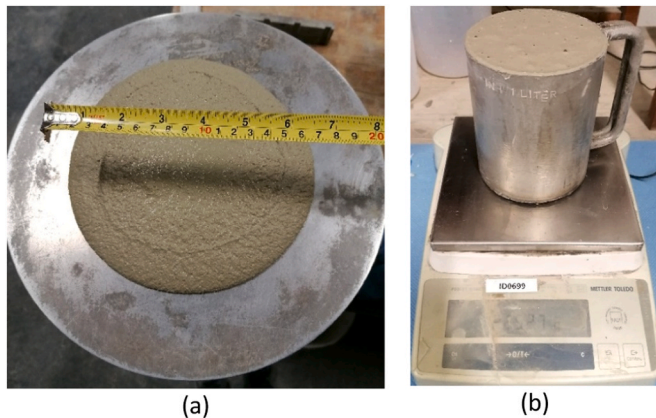

Fig. 5. (a) Spread diameter of reference mortar in the flow table; (b) Fresh bulk density measurement using a fixed volume method.

2.2.4. 3D printing process and parameters

An articulated robot (ABB IRB 1200, 5–90 IRC5) with an extruder (Makita DCG 180 RTX) of maximum dispersing force 5 KN attached to its arm was used to print sample slabs (Fig. 6). Smooth printing was achieved by coordinating both extrusion speed, defined by the caulking gun extrusion mode (Q), and the velocity of the printer head (v_n) dictated by the robot's arm movement. The extrusion speed was based on the mass increase dispensed $m_{d,i}$ over time Δt for a cartridge holder fully filled with 600 ml of fresh material. The material volume discharged per unit time (Q) of a given speed mode can be computed as follows $Q_{speed\ mode} = m_{d,i}/\rho_i \Delta t$ for each i composition, with ρ_i being the fresh bulk density of composition i. Since the extrusion flow rate is constant for the same speed mode, changes in the material do not affect the volume discharged per unit time. Therefore, a fixed Q equal to 12,654 mm^3/s has been adopted. The correlation determined the appropriate velocity of the printer $v_n = Q/ht_l$, as suggested in [38], being the wall thickness h of 40 mm and the layer height t_l 9 mm given by the rectangular nozzle. The computed velocity of 2109 mm/min was adjusted during printing to better accommodate the mix's consistency. Table 3 summarizes the printing process parameters concerning the four representative mixtures selected for printing: REF, CR51, CR67, and CR100.

Extrudability and buildability are two well-established yet descriptive requirements to consider a mortar suitable for 3D printing [ref]. It is commonly acknowledged that both properties are process and material-dependent [39,40]. Therefore, in this study, a composition is considered extrudable when it meets two criteria: (i) a single layer of 800 mm length can be extruded without clogging or segregating; (ii) after extrusion, the single filament keeps its shape with a deformation inferior to 10% of the filament width. Additionally, compositions are deemed buildable if a slab with at least eight layers of material can be printed after passing the extrusion criteria. In the case of the REF mix, the bottom layer must withstand a yield stress of at least 896 N/mm^2 at the deposition of the 8th layer. According to previous research [41,42], the yield stress at the bottom layer is calculated based on the object height H [m], density of the cementitious material ρ [kg/m3] and gravity constant g [m/s^2] (Eq.(1)):

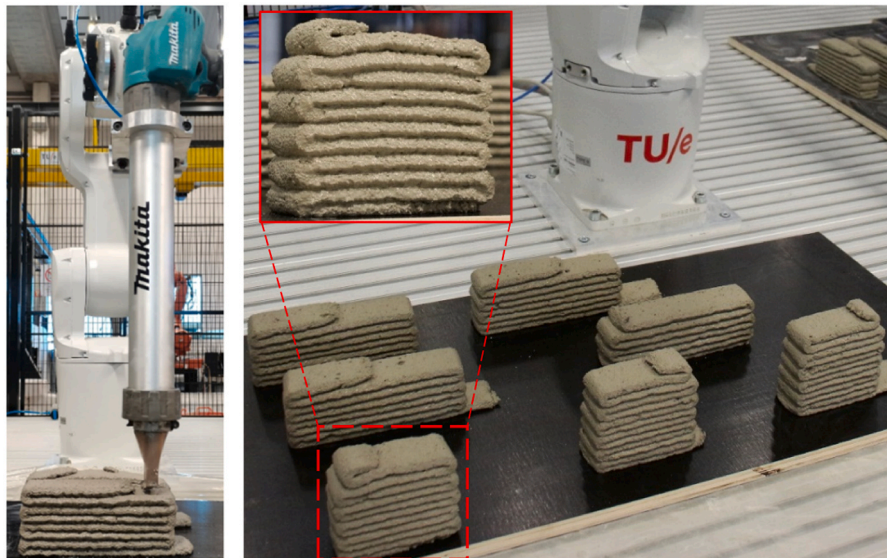$$\tau_{0,0} = \frac{\rho g H}{\sqrt{3}} \tag{1}$$

Fig. 6. Printing setup of cork mortar (CR100) consisting of an extruder attached to the print head of a robot arm.

Table 3
Printing process parameters.

Parameter	Unit			Value			
				REF	CR51	CR67	CR100
Wall thickness	mm	h		40			
Height of individual layer	mm	t_l		9			
Concrete density	kg/m^3	ρ		2155	1856	1740	1480
Velocity of printer head	mm/s	v_n	$= Q/ht_l$	35			
Material volume discharged per unit time	mm^3/s	Q	speed 3	12,654			
Adjusted velocity of printer head	mm/s	v_i		30	29	32	37
Minimum yield stress at bottom layer	N/m^2	$\tau_{0,f}$		896	771	723	615

2.2.5. Curing and preparation of specimens for testing

Once printed, the samples were covered in plastic foil for 24 hours to prevent rapid water evaporation due to early cement hydration. After one day, the printed objects were transferred to a controlled chamber with an ambient temperature of 20 °C and 60% relative humidity for curing. At 21 days, the printed samples had their cores sawn into cubes of 35×35×35 mm for compressive and splitting tension tests, yielding five cubic samples for each of the three testing directions (u,v,w). For the 3-point bending flexural, printed slabs were sawn into 35×35×160 mm samples, resulting in 3 slabs for each tested direction. Fig. 7 depicts the schematics of printed and sawn samples for testing in local coordinates. After sawing, samples were immediately transferred back to the control chamber, where they remained until the day of testing.

Cast samples of six compositions produced in standard molds of 40×40×160 mm were used to compare whether the printed process influences the mechanical and thermo-physical properties. They were cured similarly to printed samples and sawn into 40×40×40 mm cubes at 21 days for the splitting tensile test and into 30 mm thickness for the thermal conductivity test.

2.2.6. Air and oven dry densities and moisture content

The air-dry bulk density of mortars was measured after 28 days as the average bulk density of 36 specimens of each composition used for mechanical testing. Before the destructive test, all samples were weighed, their dimensions (height, length, and width) were taken in two positions, and the average volume was computed. The air-dry bulk density is calculated as the sample mass ratio by sample volume, rounded to the nearest 0,1 kg/m^3, as described in EN 1015–10 [43]. The oven-dry density of mortars was obtained from the four specimens before the thermal testing since the sample should be moisture-free for accurate thermal conductivity measurement. The mass loss is then computed as the difference between the mass reading before and after over-drying samples.

2.2.7. Scanning electron microscope, optical microscope, and mercury intrusion porosimetry

The microstructure of mortars was analyzed using two complementary microscopies: optical microscopy (OM) and scanning electron microscopy (SEM). OM displayed the general aspect of the cementitious matrix interface with cork granules using an Axiocam 310 optical microscope with a 5x magnification lens. The specimens were obtained from sawn pieces of samples tested at 28 days, carefully selected to be representative of the bulk. The remaining parts of prismatic specimens were crushed into 2–4-mm granules containing significant shredded cork pieces tangled into the cementitious matrix. These smaller pieces were used in SEM and Mercury Intrusion Porosimetry analysis.

Further investigation on the interfacial transition zone (ITZ) and crystals of the hydration product of these samples was carried out on SEM Quanta3D FEG. Mercury Intrusion Porosimetry (MIP) analyzed the mortars' pore distribution in the Micromeritics AutoPore IV 9500 Mercury Porosimeter. The four most relevant compositions selected were REF, CR51, CR67, and CR100.

When combining these observations (OM and SEM), we can see how the microstructure affects behavior on a larger scale. This is especially true for the development of an interconnected network of matrix and aggregate, which makes the material stronger, and the formation of micropores, which makes it more sensitive to temperature changes.

2.2.8. Compression, flexural, and splitting tensile tests

Mechanical tests were conducted on cast and printed samples at 28 days to assess their compressive, flexural, and spitting tensile strength. Both compressive and flexural strength were determined according to
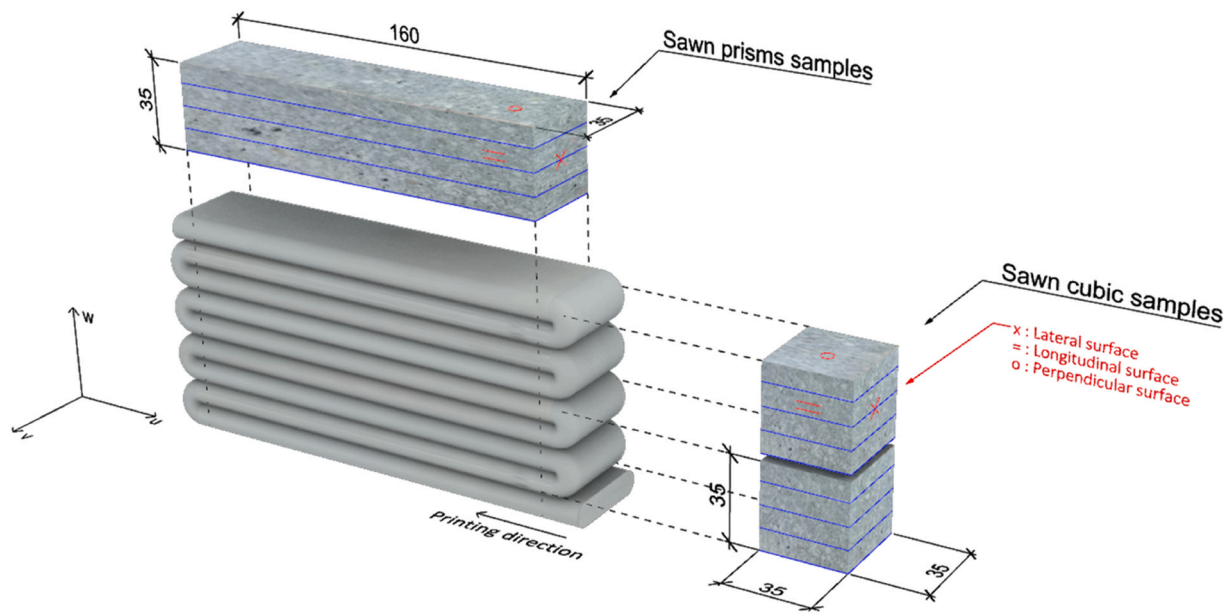
Fig. 7. Extraction scheme of sawn cubic and prisms from printed slab positioned in local axis u (longitudinal direction), v (lateral direction), and w (orthogonal direction). Prism samples were obtained individually from a single slab, while cubic samples were extracted in three pairs from a single printed slab.

EN 1015–11 [44]. The compression tests were performed in a cell-controlled tester (Controls Automax model 65-L1152/LC) with increasing loads of 2400 N/s at 40×40×40 mm cast samples and 35×35×35 mm sawn printed samples on the three loading directions (u, v,w axes). A flexural tension test was performed in an Instron 5967 3-point bending machine with increasing loads of 50 N/s in 40×40×160 mm cast specimens and 40 N/s in 35×35×160 mm sawn printed samples to guarantee an equivalent loading rate at smaller cross sections. The 3-point bending test was performed in two directions (v,w), as in Fig. 8. The split tensile test was carried out following the procedure in EN 12390–6 Annex A [45] in cubic sawn printed specimens of 35×35×35 mm in three directions (u,v,w) at 96 N/s and in cubic cast specimens of 40×40×40 mm at a 120 N/s loading rate (Fig. 9). The indirect tensile strength obtained from the splitting tensile test provides adequate information about interlayer bond strength. Table 4

summarizes tests and the number of experimental results for each composition and loading direction.

2.2.9. Thermal conductivity test by Hot Disk transient method

The thermal conductivity measurements were carried out in a Hot Disk Thermal Constants Analyzer based on the transient method complying with ISO 8302 [46]. The Hot Disk sensor consists of an electrically conducting pattern in a double spiral shape of 6.403 mm diameter, approximately five times smaller than the sample width. The distance between the sensor and the smallest sample edge, or probing depth, ensures the sensor is effectively positioned within a seemingly infinite material. The sensor, placed between two symmetrical sample pieces, functions simultaneously as a heat source, applying a heat power of 268.64 mW, and as a dynamic temperature sensor, measuring the temperature variation over 40 seconds, see Fig. 10. To test for possible
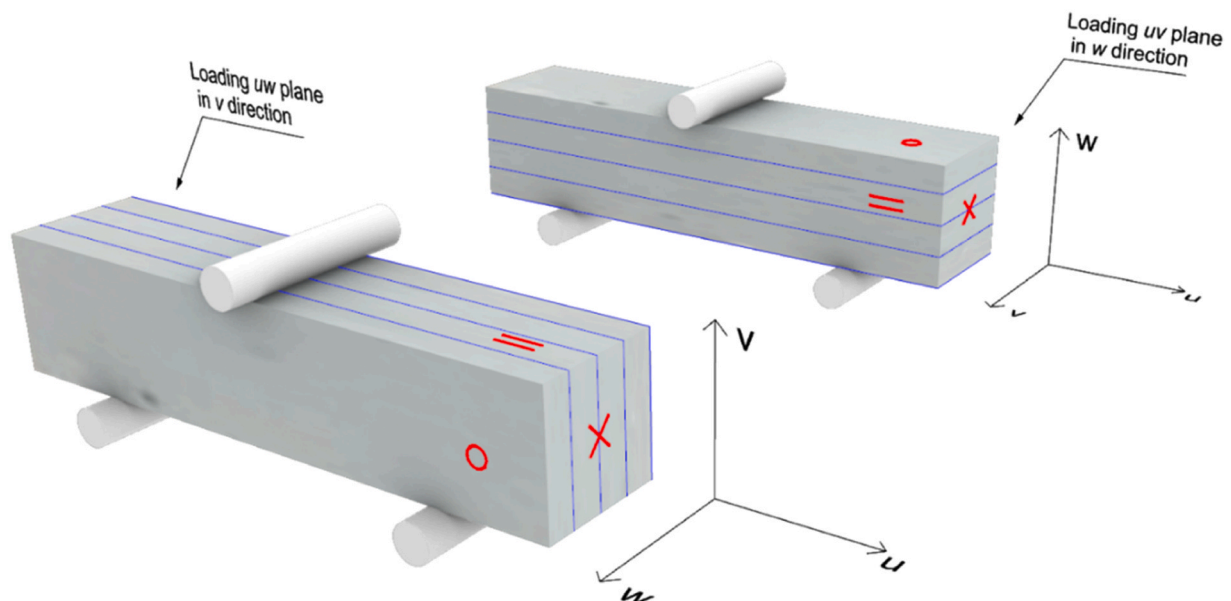

Fig. 8. Representative scheme of 3-point-bending test in sawn printed slabs of 35×35×160 mm tested in v and w directions.
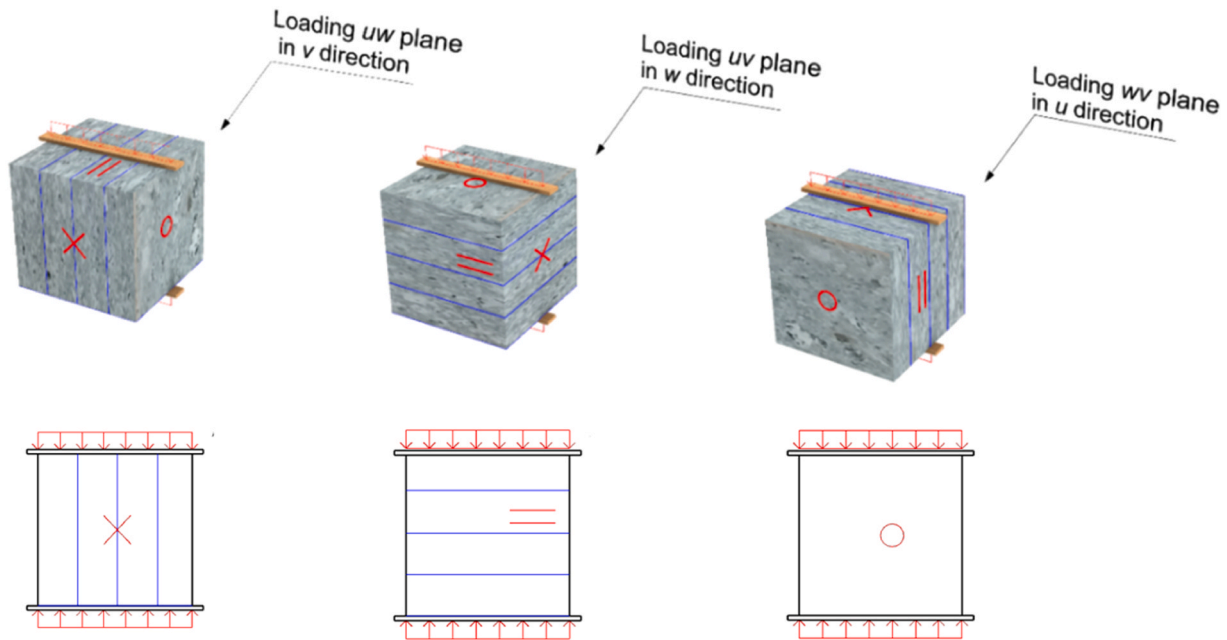
Fig. 9. Schematic representation of sawn printed samples for splitting tensile testing in three loading planes: uw (left), uv (middle), wv (right).

Table 4

Summary of experimental results, sample size, and geometry for mechanical and thermo-physical testing carried out in cast and printed samples.

Test	Test direction	Specimen type	Geometry shape and size [mm]	Loading rate [N/s]	Number of experimental results
Compression	u	Sawn	Cube of 35×35×35	2400	5
	v	Sawn			5
	w	Sawn			5
	-	Cast	Cube of 40×40×40		6
Flexural tension, 3-point bending	w.u	Sawn	Prism of 35×35×160	40	3
	v.u	Sawn			3
	-	Cast	Prism of 40×40×160	50	3
Splitting tension	w.u	Sawn	Cube of 35×35×35	96	5
	v.u	Sawn			5
	v.w	Sawn			5
	-	Cast	Cube of 40×40×40	120	5
Thermal conductivity	w.u	Sawn	Cube of 35×35×35	-	2
	v.u	Sawn			2
	v.w	Sawn			2
	-	Cast	Cube of 40×40×30		2

heat transfer anisotropy in printed samples, the thermal conductivity is measured by the unidirectional heat flux being applied in each of the three directions: axial (v-axis), tangential (w-axis) and radial (u-axis). Four cubic samples of 40×40×30 mm cast samples and 35×35×35 mm of sawn printed samples were tested, resulting in two accurate measurements of thermal response in each direction.

3. Results and discussion

3.1. Physical properties of cork granules

Table 5 displays the physical properties of GC1 and GC2. The apparent particle density (ρ_a) of both cork granules is close, with the oven-dried particle density (ρLrd) of the smaller grains of 172.8 Kg/m^3 being relatively lower than the 223.9 kg/m^3 of the larger ones. Regarding the saturated and surface dry state, GC1 has a greater particle density (ρLssd) of 613 kg/m^3 relative to 532.8 kg/m^3 of GC2. The larger specific surface area of the former particles explains the difference in densities and the greater water absorption values. As time progresses, the rate of water penetrating cells increases linearly in both particle ranges (Fig. 11), but it is approximately twice as high in GC1 as in GC2. Due to the cork's chemical composition and microstructure, water

molecules adsorb onto the surface of the particles by hydrogen bonds and accommodate into the open cells [25]. According to similar observations made by J. Chanut et al. [25], the honeycomb shape of cork cells and their textured walls are primarily responsible for this apparent hydrophilic behavior at the particle level.

It should be noted that roughly 85% of the total absorption occurs at 5 minutes in GC1 and 65% in GC2. Given that both WA$_{5\ min}$ are representative of 24-hour immersion, selecting a short immersion time of 5 minutes to pre-soak cork granules before their incorporation into the mix is advantageous. It enables quick pre-mixing of water with cork before blending it with the fresh cement paste, with minimal disturbance to the mortar's consistency. Since the mix design employs a balanced proportion of both granules, the mean WA$_{5\ min}$ value of 200% by LWA weight was adopted to partially saturate the LWA.

3.2. Influence of cork on mix consistency and fresh bulk density

The rheological profile of mortars is illustrated in Fig. 12 by the spread flow diameter. The graph shows that the mix consistency changes over time, which varies more significantly in cork mortars. Three ranges of flow development are identified and associated with cork absorption. The first one occurs within the first five minutes after mixing. In this
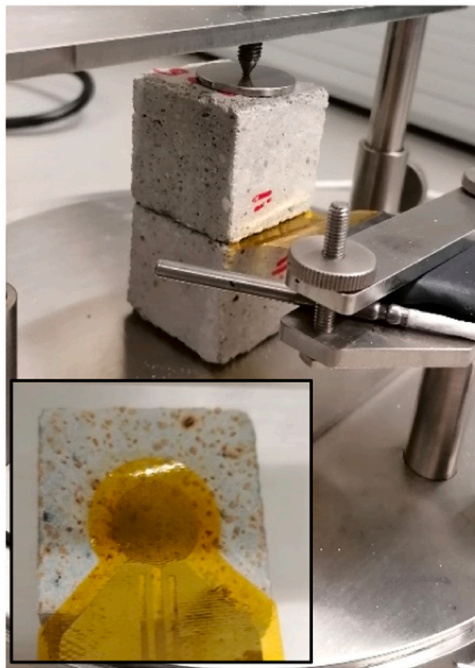
Fig. 10. Double spiral sensor centrally positioned between two flat surfaces of a printed sample, in the example of CR51, to measure the thermal conductivity using the transient method perpendicular to the printing direction (heat load applied onto the w-direction). The sensor of 6.403 mm diameter is sufficiently small to guarantee the infinite material assumption for unidirectional heat flux calculation.

Table 5

Physical properties of granulated cork with particle sizes 0.5–1 mm and 1–2 mm.

Cork granule size	GC1		GC2	
	Mean	Std. dev.	Mean	Std. dev.
Apparent particle density, ρ_a (kg/m^3)	309.3	0.006	324.5	0.012
Oven-dried particle density, ρ_{Lrd} (kg/m^3)	172.8	0.002	223.9	0.005
Saturated and surface dried particle density, ρ_{Lssd} (kg/m^3)	613.0	0.006	532.8	0.015
Absorption 5 min, WA$_{5\,min}$ (%)	216	0.3	86	1.4
Absorption 60 min, WA$_{1\,h}$ (%)	248	29.9	90	23.8
Absorption 24 h, WA$_{24\,h}$ (%)	254	0.3	138	1.4
Porosity, P (%)	44	0.5	31	1.0
Loose bulk density, ρ_b (kg/m^3)	105.4	0.8	108.3	0.3
Voids, v (%)	39.0		51.7	

Fig. 11. Mass increase evolution in cork granules over 48 hours of immersion in water observed in the tea bag method.

Fig. 12. Consistency changes considerably in cork mortars over time associated with cork's absorption and advancement in cement hydration.

short period, the water provided to the cork positively contributes to higher flows since it remains free at the cork's surface and cement paste. However, due to the dispersing effect of excessive water, the consistency is too fluid to be printable. Thus, a spread flow of 180 mm determines the high limit of the printability window. At the start of printing, at five minutes, the consistency rapidly drops to a uniform spread over formulations, converging to values between 163 and 170 mm, sufficient to provide proper cohesion for the extruded layer. During the initial state, the cement paste started to set as well, as observed by a reduction in diameter of the reference. It can be concluded that the flow decrease in cork mortar combines continuous free water absorption by cork with cement setting.

The second stage, from 5 to 45 minutes, is followed by an accelerated decrease in the spread flow of cork mortars, where the ones with higher content (CR34, CR 51, CR67, and CR100) displayed worse flowability than the reference. Interesting to notice that the superplasticizer content also had an impact on retarding the decrease of flow over time. This
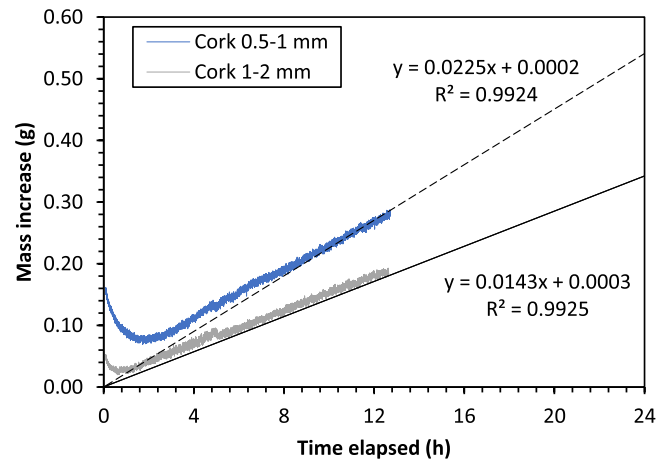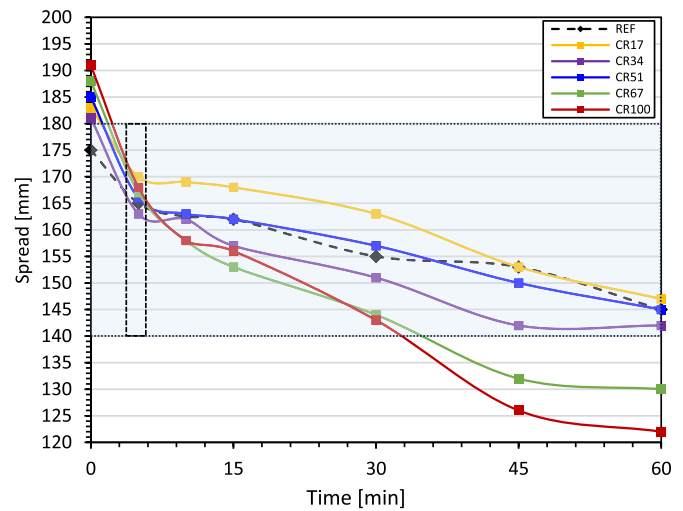
distinction is evident in similar superplasticizer contents in combination with lower cork mixes, such as CR17, when compared to CR34 and CR51 concerning CR67 and CR100. Both CR17 and CR51 are turning points where the compositions have similar superplasticizer content as their higher cork counterparts. However, the absorption effect over time is less significant due to the lower cork fraction.

After 45 minutes, mortars enter the final stage, where the cement setting, due to advanced hydration reaction, overcomes the absorption capacity of cork, slowing down the spread reduction. Currently, the lightest mortars (CR67 and CR100) have considerably developed their yield strength, associated with a significant spread decrease, and are no longer printable. Meanwhile, for lower cork percentages, mixes are still extrudable. Hence, a spread flow of 140 mm determines the lowest bound for the printability window.

Other studies reported that mixtures attaining spread flow values between 130 and 210 mm were thought to be better for printing [47]. This study demonstrates that the printability limits are narrow, with the spread falling between 140 and 180 mm, and for best printing quality, it should be aimed at 160 mm. For this range, compositions have a low enough yield strength that they are not prevented from flowing under the 5 KN force of the extruder. Overall, until 30 minutes, mixtures attained a uniform plastic consistency due to spreads within 140 and 200 mm intervals as described in EN 1015–10 [43].

It is worth mentioning that since a rise in the water-to-cement ratio w_t/c is well recognized to influence both rheological and mechanical characteristics [48,49]; keeping it constant across compositions allowed us to evaluate the effect of cork addition on both properties with minimal disturbance of the increase in water content. Another study demonstrated that superplasticizer and cork content, expressed as increments in water absorption, strongly influence the flow regime by considerably decreasing mortar's yield stress [49]. Despite adopting a fixed w_t/c ratio of 0.36 composed of the w_{eff}/c and wa terms that were aimed to minimize this influence, the water provided for saturation inevitably resulted in higher flows shortly after mixing (Fig. 13). Nevertheless, at the printing time, a slightly softer consistency of lighter mortar positively affected the printing quality. The interaction of superplasticizer and cork content, expressed as increments in water absorption, has been demonstrated to influence the flow regime by considerably decreasing mortar's yield stress.

The fresh bulk density of the mixtures linearly decreases with increments of cork, as depicted in Fig. 14. Because the mortars' density is directly related to the volume fractions and densities of the constituent components, when cork assumes a larger share of the aggregate volume, its lower density ($0.172 \, g/cm^3$ - $0.224 \, g/cm^3$) compared to sand's ($2.65 \, g/cm^3$) contributes proportionally to a decrease in the fresh density of the mortars. The standard mixture possesses a normal-weight density of $2155 \, kg/m^3$, gradually diminishing as cork granules increasingly replace quartz sand, as exemplified by the $2042 \, kg/m^3$ density at 8% vol cork (CR17).

The shift from normal weight to lightweight mortars occurs at 15% vol cork content (CR34), marking a $1955 \, kg/m^3$ density. At 30% vol cork concentration (CR67), the mortars' density achieves its threshold of $1740 \, kg/m^3$, beyond which the density marginally declines to $1480 \, kg/m^3$ upon complete replacement of sand with cork in the lightest mortar (CR100). This lightest mortar variant represents a remarkable 32% reduction in self-weight compared to the reference value.

3.3. Effect of increasing addition of cork on printing quality

In the context of the extrusion process, the material must comply with two main requirements to be considered printable after conveying the print system. The first requirement, extrudability, describes the material's ability to leave the nozzle smoothly as a continuous filament with unrestricted material flow. This is achieved if the material holds sufficient viscosity and dynamic yield strength to remain cohesive under
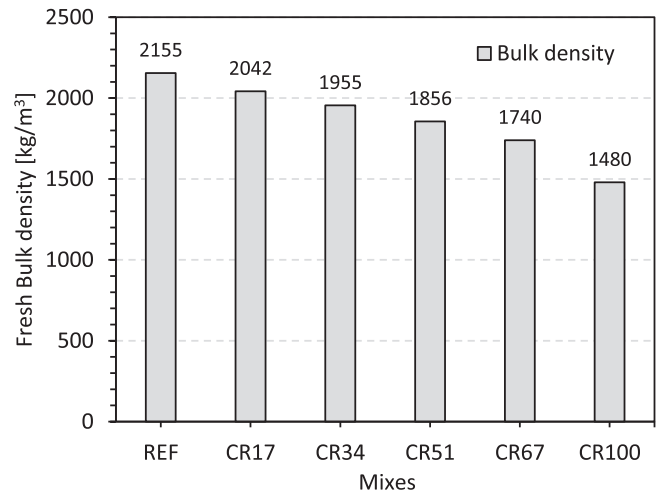

Fig. 14. Reduced fresh bulk density of printed mortars due to higher sand replacement by cork.

the pump pressure or conveyor system. Extrusion was successful due to the plastic consistency of the mixes targeted in the mix design. Both cork and sand mixes conveyed the extruder continuously and cohesively, so bleeding and segregation did not occur throughout the printing. Upon placement of the first filament, mixes retained their shape with a minor 10% spread, thus meeting the extrudability requirement.

The second criterion relates to the material's capacity to withstand the weight of successive layers accumulated by the printing method [39, 50,51] without significant deformation of filament height. As presented in Fig. 15, sand (REF) and cork mixes (CR67 and CR100) continuously exited the rectangular nozzle in bonded layers, with their filaments maintaining a stable shape. Layers of the original 9 mm height were stacked upon each other until they met the print object height. When the printed object meets the target height, the gravity-induced stresses reach their maximum value at the bottom layer. The reduced size of printed slabs (both short height and length) resulted in a relatively fast buildup rate, which is proportional to the rate of weight increase due to the increment of layers over the printing time. Since these stresses did not exceed the static yield stress at the bottom layer, plastic collapse did not occur, allowing for stable, slender slabs.

Providing that the minimum yield stress needed to bear the load of
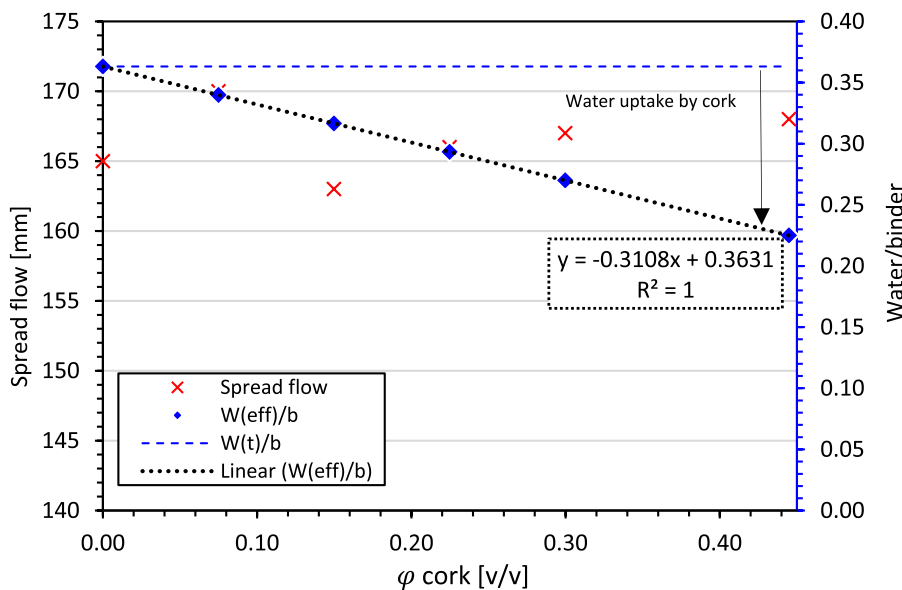

Fig. 13. Effect of increasing pre-soaked cork content on the effective w/b ratio and spread flow at the start of printing 5 minutes after mixing.
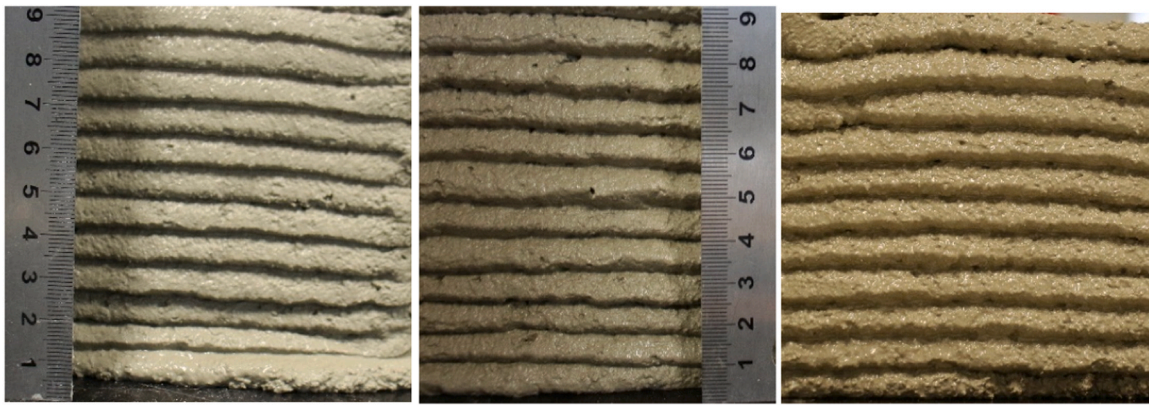
Fig. 15. Printed samples show a satisfactory layer buildup of 11 layers in the example of reference (left), CR67 (middle), and CR100 (right).

successive layers at the base of a print slab is directly linked to the material density, as specified in Section 2.2.4, a lighter mortar, for a fixed yield strength, can accommodate 46% more vertical layers over the same length. Consequently, opting for lighter mortars like CR67 and CR100 under comparable consistencies proves advantageous over REF in producing taller objects.

Regarding system parameters, increasing the cork content allowed for higher printing speeds with minimal impact on print quality. The lightest mix (CR100) had its printing speed adjusted by 7 mm/s compared to the reference mixture. This adjustment could lead to a total linear distance of 25 m printed over an hour, provided that increasing cork content also leads to a faster mortar stiffening and development of the yield stress (Section 3.2). Its lower packing density due to the absence of fine sand, softer consistency, and lighter weight confers CR100 with the ability to be printed more rapidly (Fig. 16). The lack of sand widens the distance between the mortar components, fine cement, and larger cork granules, and when associated with the release of free water by cork, causes a decrease in the mortar's yield stress.

3.4. Microstructure of cork mortars

The macrostructural analysis of the mortars reveals the presence of discernible macropores exceeding 0.1 mm in size, resulting from compacting the cast samples, as shown through the prism surfaces in Fig. 17 (a). Subjecting LWAC to mild compaction energy can adversely affect its uniformity, potentially leading to material segregation due to inherent density disparities [52]. Conversely, applying 3D printing technology to create similar structures could be beneficial to mitigate air voids through controlled material conveyance and sequential deposition. This benefit is clear from Fig. 17(b), which shows the cross-sectional view of printed specimens. A noticeable decrease in large air voids is visible, which differs from how cast samples usually look.

MIP and SEM analysis identified which aspects of solid content, the hydration products of cement, aggregates' microstructure, and voids

influenced the mechanical and thermo-physical properties of the studied mortar, such as strength, drying, and thermal conductivity. The selected mixtures, namely REF, CR51, CR67, and CR100, exhibited a progressive increase in void content (Fig. 18), contributing to the lower bulk and apparent density of cork mortars, as detailed in Table 6. The following sections explain how the porosity of these mixes impacted their strength and thermal conductivity. Nonetheless, mortar's porosities are considerably low (below 30%) due to its modest w_t/c ratio.

Fig. 19 shows interesting aspects of pore size distribution in the hydrated cement paste of the tested mortars. An increased quantity of incorporated cork led to a marked elevation in the overall volume of pores spanning dimensions smaller than 10 nm, 50 nm, and 8 μm, depicted as peaks in the mercury intrusion volume within these respective pore ranges. In contrast, the reference mixture displays a lower overall pore volume. Regarding pore dimensions, it is pertinent to classify capillary voids into two subcategories: medium capillary pores, encompassing diameters ranging from 10 to 50 nm, and large capillary pores, which include diameters surpassing 50 nm. Prior research has indicated that capillary pores exceeding 10 nm predominantly impact material strength and permeability. In contrast, gel pores measuring less than 10 nm influence drying shrinkage and creep behavior [48].

The current study assumes a similar premise, asserting that pores measuring less than 15 nm significantly impact cork mortars' compressive, flexural, and tensile strength concerning the reference. The volume of medium-sized pores, spanning the range of 50 nm to 15 nm, emerges as relatively insignificant when comparing CR51 and CR67 to the REF mixture and slightly more prominent in the case of CR100.

In Fig. 20(a), the results of slag cement hydration are shown as a cementitious matrix made up mostly of calcium silicate hydrate (C-S-H) and minor compounds of calcium hydroxide (C-H). It is possible to notice the presence of some micropores and a dense interfacial transition zone (ITZ) between hydrated cement paste and sand grains. In the presence of cork, as is the case with CR51 in Fig. 20(c) and CR100 in Fig. 20(d), a few more micropores are present in the cementitious paste.
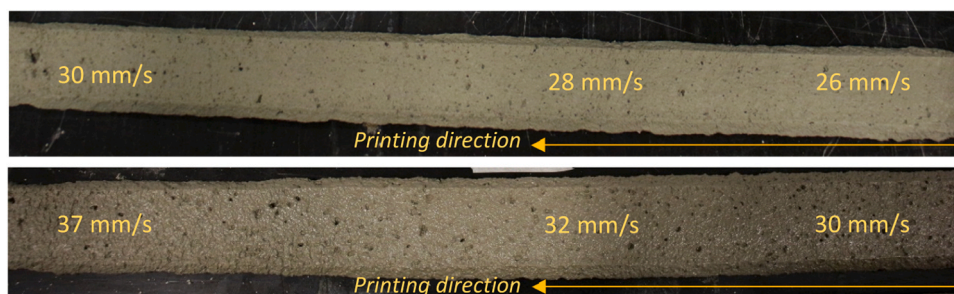

Fig. 16. Extrusion of a single filament in the case of reference mix (above) and CR100 (below) show similar printing quality at different speed conditions. Due to slightly higher flowability, lighter cork mortars required faster printing.
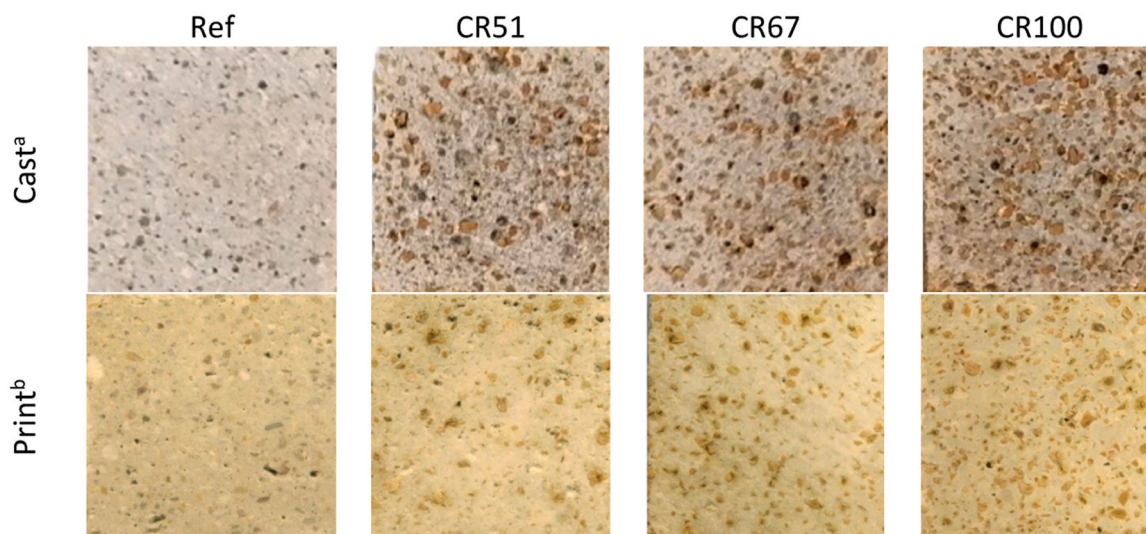
Fig. 17. Cross section of print samples with increasing cork content from left (Ref), middle (CR51 and CR67) to right (CR100) show fewer pores in the cement matrix compared to cast samples.
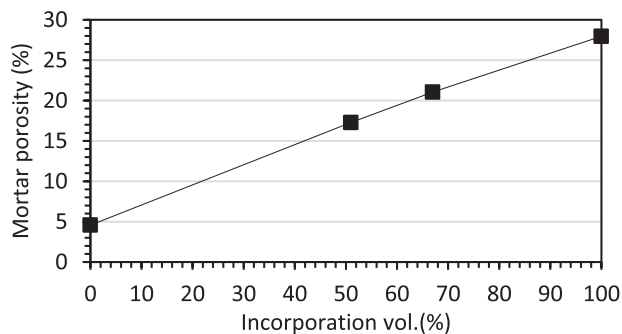

Fig. 18. Porosity of mortars with increase in cork content.

Table 6
Porosity values of reference and cork mortar samples at 28 days.

Sample names	REF	CR51	CR67	CR100
Porosity (%)	4.57	17.28	21.05	27.96
Median Pore Diameter (Area) (nm)	7.1	8.1	8.0	7.4
Bulk density at 0.1 MPa (g/ml)	2.32	1.99	1.87	1.58
Apparent Density (g/ml)	2.42	2.35	2.31	2.12
Average pore diameter (nm)	29.8	24.4	25.4	32.2

Cork's cellular structure increases the surface area that interfaces with the cement paste. This creates an appropriate ITZ with a good bond between the cork and cement matrix, as presented in Fig. 20(e) and detailed in Fig. 20(f). Overall, sand and cork mortars demonstrated well-developed hydration products at 28 days and pore dimensions consistent with MIP measurements.

If the cork granules are smaller, it implies a higher specific surface area. This increased surface area can enhance the contact between the cork granules and the cement matrix. A larger ITZ can be beneficial for improving the overall performance of the concrete because it allows for better adhesion and interaction between the cork and the cementitious material.

The extension of ITZ is greater for the smaller cork's granule size due to their higher specific surface area, which greatens the contact with the cement matrix. For the same reason, these tiny granules attain a higher absorption. Once the concrete has set, the cement particle slowly consumes the water used to fill the cork's surface due to a difference in relative humidity (relative pore pressure or water activity) between cement paste and LWA [53].This migration of water occurs through small pores located at the paste, which pull moisture from the surface of the LWA through capillary pressure. Internal curing promoted by cork's saturation is particularly interesting in the hydration of slag cement. Because its initial low-rate hydration results in a system of capillary pores that, under drying conditions, allows quick water loss, hindering the formation of hydrates. Several days after placing (casting or printing), the concrete may acquire a bluish hue due to the reaction of iron sulfide in the slag. Generally, the bluish tinge disappears after a few days, provided the concrete has been exposed to air [53]. Otherwise, the oxidation may be prevented. The degree of moisture content in cork and slag cement composite can be observed by the changes in hue within the cementitious matrix. Fig. 21 shows the effect of higher saturation zones around the cork that provided water to the cement matrix and, therefore, had an accelerated evaporation and oxidation process once the surface had been exposed to air. At the same time, the core remained relatively moist, displaying a dark hue.

3.5. Dry bulk density of hardened mortars

The air-dry density of mortars after 28 days of curing diminishes as the proportion of cork additives rises. In Fig. 22, the print reference mortar exhibited a density of 2131.6 kg/m^3, whereas its counterpart containing only cork displayed a markedly 31% lower density of 1469.6 kg/m^3. At intermediate cork volume fractions, the air-dry densities were 13% and 19% less than the standard. Notably, the printing procedures did not significantly influence the sample densities, where any minor difference in cast ones stems from a lower void content due to the segmentation of layers, as explained in Section 3.4.

Owing to the mass loss through the evaporation of unbounded water molecules, oven-dry densities are smaller than air-dry densities. As expected, this difference increases with a larger cork content. Because cork is pre-wetted before placement into the cementitious mixture, it serves as a reservoir that readily releases water for hydration or replaces moisture lost through evaporation or self-desiccation in the mortar's hardened state [54]. Generally, in ambient conditions, the water entrained in LWA pores, ranging from 5 to 300 micrometers, moves to finely developed hydrated cement pores smaller than 1 micrometer [55]. This phenomenon, referred to as internal curing, has been reported to reduce microcrack formation in the cement matrix and improve the integrity of the transition zone at the LWA interface [55,56]. Under drying conditions, the remaining free water moves through capillarity
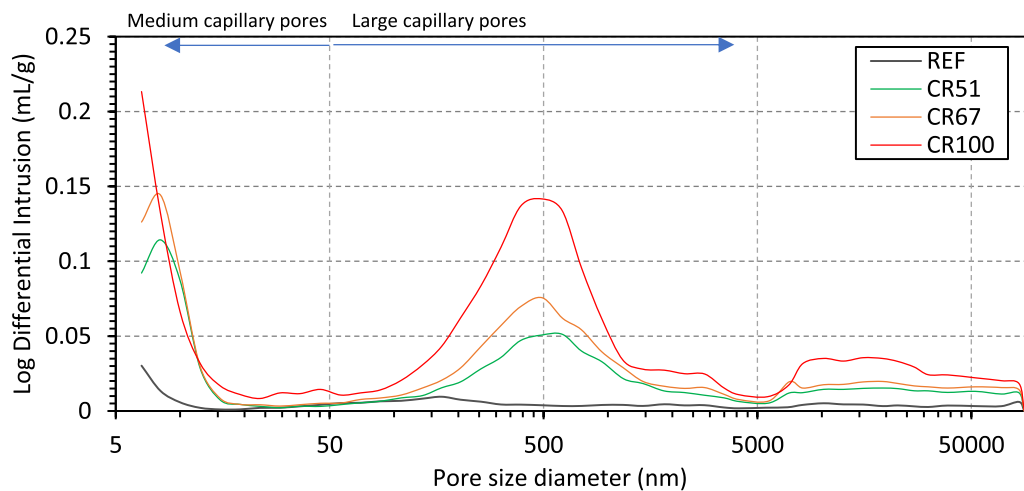
Fig. 19. Pore size distribution of mixes with w_t/c 0.36 at 28 days measured by MIP.

action to the surface, where it evaporates, resulting in a relative mass loss proportional to increments in cork concentration (Fig. 23).

While the printed reference with a ρ_{OD} of 2064.8 kg/m³ is only 3% less than its air-dry density, at 44% vol of cork, this gap doubles. For intermediate cork volume fractions, such as 22% and 30% by volume, the oven-dry densities of the printed samples were recorded at 1791.5 kg/m³ and 1630.5 kg/m³, being 4% and 6% below their air-dry densities, respectively. The mortar containing the highest proportion of cork attained a ρ_{OD} of 1363.0 kg/m³, which is 34% lower than the reference sample.

Based on the empirical data, the oven-dry density of mortars is given as a function of the volume fraction of cork as follows: $\rho_{dry} = -1418\varphi + 2128$, where ρ_{dry} is the mortar's dry density relative to the volume fraction of cork φ. The decrease in the self-weight of cork composites is attributed to the cork's cellular structure, which consists of about 93% air [26]. Notably, the density of the cork-based mixture aligns with that of lightweight aggregate compositions incorporating materials such as expanded clay [57] and expanded perlite [11,58], thereby underscoring the potential of cork as a viable alternative to these conventional aggregates.

3.6. Compressive strength

An exponential variation in the compressive strength of samples with an increase in cork's fraction is presented in Fig. 24. As the percentage of cork rises, the strength of printed and cast samples decreases proportionally. While the reference cast sample attained a load-bearing capacity of 58.3 MPa, at 7% vol and 15% vol of cork, it reduced to 51.1 MPa and 41.1 MPa, respectively. Given their compressive strength and densities more significant than 40 MPa and 1800 kg/m³, these compositions fall into the structural lightweight aggregate concrete category according to ACI [3]. At more significant volume fractions of cork, as in 22% vol and 30% vol of cork, the mortar's strength is 36.9 MPa and 30.7 MPa, respectively. The lightest mortar with 44% vol cork obtained a compressive strength of 21.1 MPa. Although 64% weaker than the reference, its compressive strength is sufficiently structurally sound for constructing 3D-printed load-bearing walls in low-rise residential buildings. In respect to the aggregate type, all cork mortars developed in this study, in particular CR100, demonstrated superior compressive strength to those of tire rubber mortar (RP25-RG75) of similar density [14], and waste glass mortar (G50-ETM) [12].

Contrarily to casting, printing disregards external compacting or vibrational energy to produce a solid sample. By exerting pressure onto the fresh mortar to extrude a single filament, the piston forces the exit of

entrapped air voids in the lateral and longitudinal printing directions. As a result of continuously segmenting the sample's core into thinner filaments, the lightweight aggregates become uniformly distributed over the sample's height. This limits segregation and reduces the formation of air voids between aggregate and matrix, thus improving the cementitious matrix and LWA bond. This decrease in voids, early demonstrated by a slightly greater density in printed samples, explains a superior load bearing capacity in both u or v directions of printed lighter mortars (CR67 and CR100) compared to their cast counterparts, and slightly less prominent in the u direction for the hybrid mortar (CR51).

Overall, the printing process did not negatively influence the load bearing capacity of printed mortars containing cork. In fact, except for the reference, all compositions attained a slightly greater compressive strength in at least one of the loading directions compared to the cast ones. Inevitably, printed samples displayed anisotropic behavior under compression stresses, given that the ultimate strength in at least one direction deviates in a few megapascals from the mean of the other two directions. It can be argued that the difference in the compressive strength of printed mortars between axial and lateral loads are withing the scatter of results, with the orthogonal direction overall showing lower compressive strengths.

The failure mechanism under uniaxial compression in the LWAC slightly differs from that of normal weight concrete (NWC). The deformability, and consequently the rigidity of the components and internal adhesion, determine how forces are transmitted in concrete [59]. Because lightweight aggregate particles are softer than the surrounding mortar ($E_{particles} < E_{mortar}$), they do not engage fully in the transmission of internal forces [3,48]. When LWAC is loaded under uniaxial compression, compressive stress trajectories are transmitted in the cement matrix and run around the aggregate, creating orthogonal tensile stresses for applied loads at the vicinity of the LWA. When the LWA reaches its ultimate tensile strength and failures, the cracks spread to the cement paste. Thus, in general, for LWAC, the weakest phase is the LWA and not the ITZ [60]. In the case of concrete containing cork, however, the quality of ITZ plays an essential role. Within the same composite, cork granules promote varying conditions for developing a denser or poorer ITZ. As a natural product, there are unavoidable changes in the chemical composition proportions, particularly the presence of more hemicellulose in some cork granules due to extraction region. It has been reported that higher hemicellulose fractions may delay and hinder cement hydration, which could be one reason for debonding the ITZ at some locations [22,61]. The other aspect has to do with cork's absorption, which results in variations of its volume, swelling when wet, and shrinking after drying. This promotes cork cracking and decohesion on the cement matrix [18]. Finer granules that
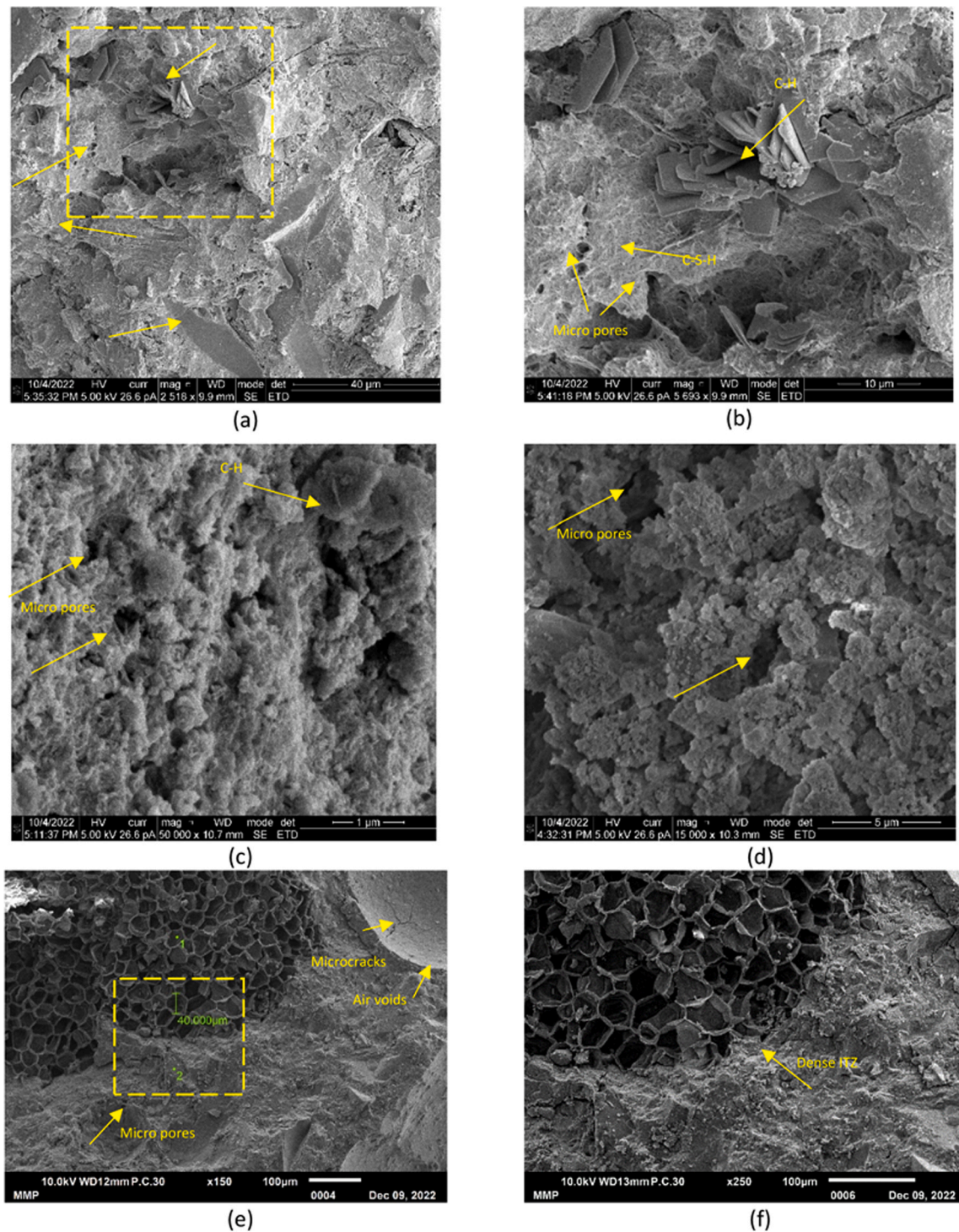
Fig. 20. (a) SEM image of the cementitious matrix of REF showing micropores and hydration crystals. (b) Detail of hydration products and micropores in REF. (c) Presence of micropores in cement paste of CR51 and portlandite. (d) Presence of micropores in cement paste of CR100. (e) Cementitious matrix of CR100 shows micropores and the cellular structure of cork benefiting a proper bond with cement paste. (f) Detail of ITZ cement and cork.

attain higher specific surface area are subjected to more sever volume variations. As an example, Fig. 25 shows how the crack initiates tangent to the poor ITZ, which decohesion between cork and cementitious matrix occurred and propagates through the latest to the nearest cork granule circumjacent by a dense ITZ, contouring the stiff sand particle.

3.7. Flexural and tensile strength

The flexural strength followed a similar exponential decrease with a rise in cork's volume, as observed for compressive strength since factors such as the content of capillary voids affect both properties similarly (Fig. 26). The lightweight mortars attained a flexural strength of approximately 15% of their compressive strength. In contrast, the ratio was about 10% in the reference. The reference mortar reached a flexural
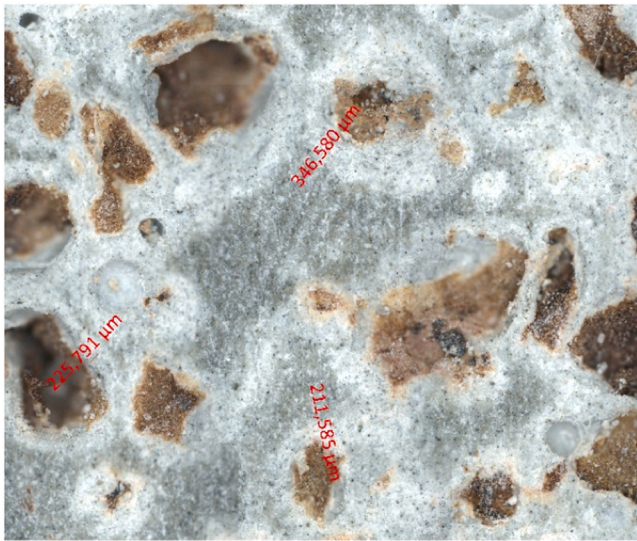
Fig. 21. Contrast of hue in slag cement containing partially saturated cork granules. Lighter grey clusters surrounding cork particles display an advanced oxidation process of slag cement after hydration at contact zones. The bluish hue between clusters is due to the reaction of iron sulfide in the slag, which has not yet oxidized. Example of CR100 mortar with cork granules of approximately 500 μm displaying an ITZ offsetting by 346 and 211 μm, and 1000 μm granule by a 225 μm ITZ.
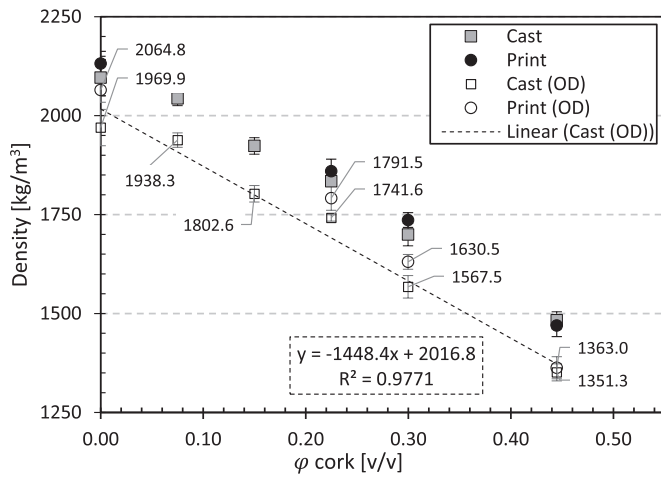

Fig. 22. Oven dry and dry densities of cast and print samples with increase in cork's content.

strength of 9.9 MPa, while the lightest cork mortars reached 3.4 MPa, and for intermediate compositions, these values are exponentially distributed between 9.3 MPa (CR17) and 5.6 MPa (CR67). Generally, no significant difference was observed in the flexural capacity of the cast and the v direction of the printed sample. However, at orthogonal loading (w direction), the flexural strength was slightly superior to that of cork mortars.

Regarding the splitting tensile strength, the load-bearing capacity also reduces as the cork's volume increases (Fig. 27). All printed compositions exhibited mild anisotropy, with a tensile strength slightly superior in v and w directions. The differences regarding cast samples were minor. Given that the variation in tensile strength within each direction is less than 1% compared to the cast samples and the other two directions, it can be considered negligible. Among the mortar compositions, the CR100 variant, characterized by its lower density, demonstrated a tensile strength of 2.5 MPa in both the v direction and
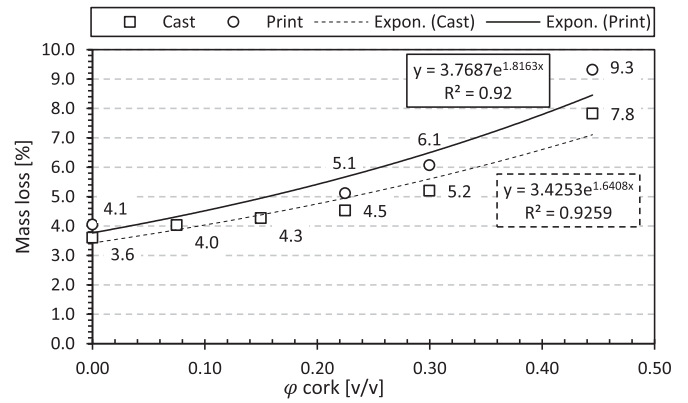

Fig. 23. Additional unbound water onto cork granules leads to a higher mass loss during drying.

the cast sample. On the other hand, CR51 and CR67 achieved higher tensile strengths of 4.7 MPa and 3.7 MPa, respectively, compared to the reference strength of 6.3 MPa in a similar direction. These results show that the printing method has no large effect on the mechanical strength of the printed samples. The failure pattern depicting a rupture coincident with the application of the load (Fig. 28) guarantees the validity of the results with a premise homogeneity of the sample.

3.8. Thermal conductivity

Thermal resistance is an important parameter to determine the energy loss through a building element, mainly through conduction. The thermal resistance is computed as the ratio between layer thickness and the material's thermal conductivity. It is well known that the material must have reduced thermal conductivity values to reduce energy loss.

As expected, the thermal conductivity values (λ-values) exponentially drop with increments of cork, as shown in Fig. 29. This reduction follows the decrease in the mortar's self-weight demonstrated in Section 3.5. Denser mortars attain higher thermal conductivity values, as in REF with 1.52 W/mK, CR17, and CR34 with 1.44 W/mK and 1.26 W/mK, respectively. Above 51% replacement of sand by cork, the λ-value falls to 0.96 W/mK and reaches 0.82 W/mK at CR67, mainly relying on cement paste's conductivity. When cork replaces fine sand entirely, this value drops by half, reaching 0.40 W/mK at CR100. This lightest mortar has a λ-value 74% lower than the reference.

The 3D-printed samples yielded similar thermal conductivities relative to the cast samples, making the minor differences insignificant. Given the analogous λ-values in all three directions, the hypothesis of homogenous and isotropic heat propagation in the media holds.

The insulation capacity of cork-only mortar is superior to values obtained by incorporating expanded glass beads [12] and tire rubber [13,14] into 3D mortars. The analyzed data agrees with an exponential regression of the thermal conductivity λ in W/mK as a function of the volume fraction of cork φ, in the range $0 \leq \varphi < 0.61$. This relationship can be expressed as $\lambda(\varphi) = 1.763 \cdot e^{-2.939\varphi}$ with a R^2 value of 0.9188.

Regarding thermal resistance, lighter mortars require a wall thickness approximately 74% thinner than the reference to achieve a similar value of 4.7 m²/W.K, as specified in the Dutch building code for insulation of external walls [62].

4. Conclusion

This work focused on the development of lightweight and low-conductive mortars for 3DCP, where scraps from bottle stopper production were used as lightweight aggregate. Cork granules between 0.5 and 2 mm were employed in increasing replacement rates (0, 17, 34, 51, 67, 100%) of quartz sand to produce printable mortars. The physical
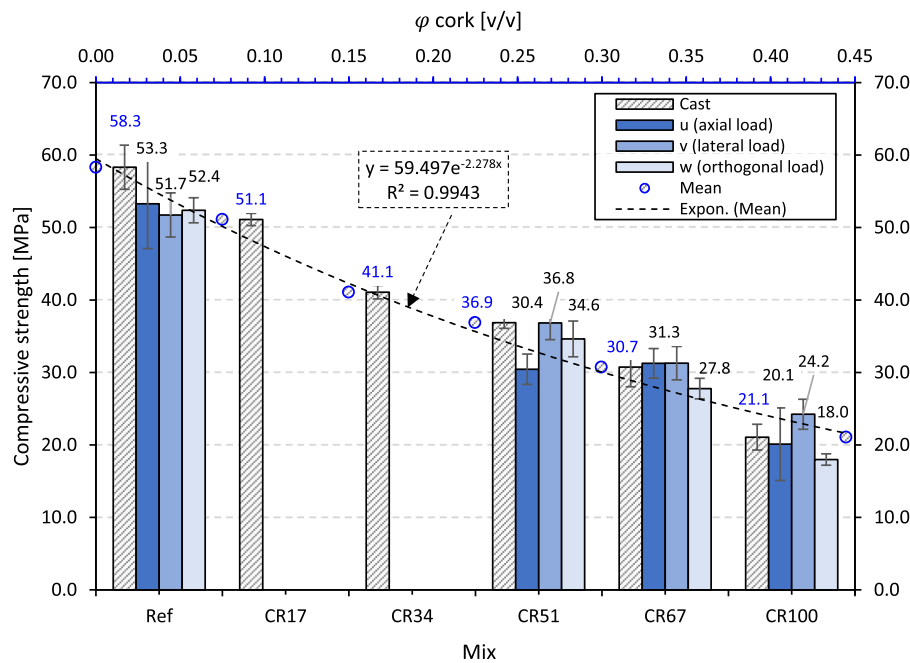
Fig. 24. Variation in compressive strength with increase in volume content of cork in cast and printed specimens.
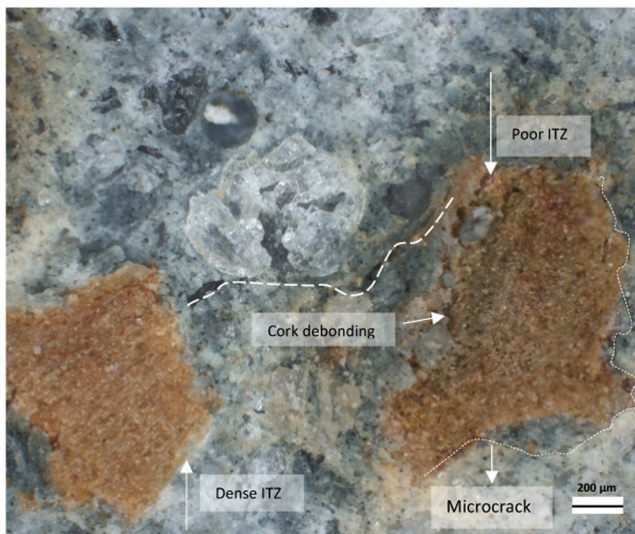

Fig. 25. Fracture pattern of print sample under uniaxial compression. Crack is initiated at adjacency of the lightweight aggregate and runs through the cement matrix until the nearest lightweight aggregate granule, contouring sand particle in CR51 mix.

characteristics of cork granules, such as bulk and particle density and water absorption, were quantified to understand their effect on the mix design. Key printing parameters (i.e., velocity of printer head, material volume discharged per unit time) were defined based on the mortar's fresh state (i.e., consistency and bulk density). The effect of cork, as a lightweight aggregate, on the mortars' printability and buildability was investigated. In the hardened state, the impact of cork on the microstructure, thermal-physical properties, and mechanical properties of both printed and cast samples was assessed. The study unveiled the following:

1) In the fresh state, introducing cork granules did not negatively affect the consistency of mortars. By incorporating pre-soaked cork and keeping a fixed w_t/c ratio, all mortars attained optimal workability for printing.

2) Cork mortars reduced the required yield stress at the bottom layer due to lower fresh bulk densities. That containing 100% cork attained a fresh density of 1480 kg/m^3, representing a 32% reduction in self-weight and, consequently, in the minimal yield stress compared to the reference.

3) An increase in cork addition similarly influenced densities in the hardened states. With 15% vol of cork, the composites enter the lightweight range of mortars and concrete.

4) The macrostructural study revealed that the printing process reduces macropores in the sample's core relative to the compaction of lightweight aggregate mortars. The mortar's microstructure showed a dense ITZ between the cork and cementitious matrix, with most micropores in the matrix. Although ascending cork contents increase porosity, all mortars obtained low porosity values ranging between 5% and 30% due to a low w/c ratio.

5) Despite the reduction in mechanical strength compared to the reference mortar, all cork composites presented adequate mechanical properties for a structural lightweight aggregate concrete of up to 15% vol cork and as lightweight aggregate concrete of up to 44% vol cork. For instance, the compressive strength ranged from 21.1 MPa at 100% cork to 51.1 MPa at 17% cork compared to 58.3 MPa in the reference mortar. Both flexural and tensile strength followed a similar reduction as the compressive strength.

6) Given the minor difference in load-bearing capacity between print and cast samples, the printing process did not significantly influence printed mortars' strength development. All mortars attained proper interlayer bonding strength, with a minor distinction in all three directions.

7) Augmentation of cork into the cement matrix significantly improved the thermal conductivity values. For instance, while the standard mortar bore a λ-value of 1.42 W/mK for a high amount of cork (50, 67, and 100%), the mortars showed acceptable thermal conductivity values ranging between 0.40 and 0.96 W/mK. The thermal conductivity was reduced by 74% at the highest cork content compared to the standard mortar.

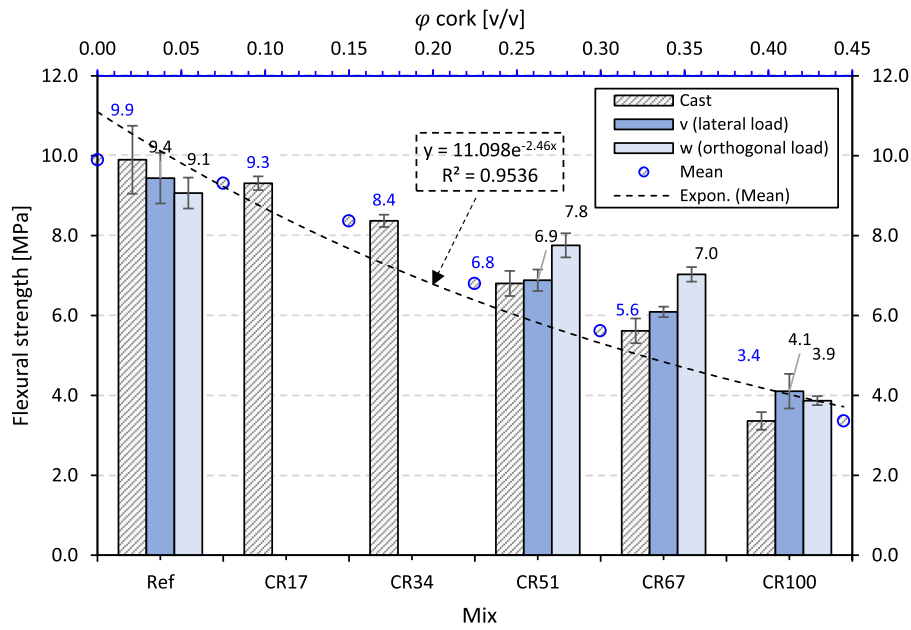Overall, this study on incorporating cork into a cementitious matrix

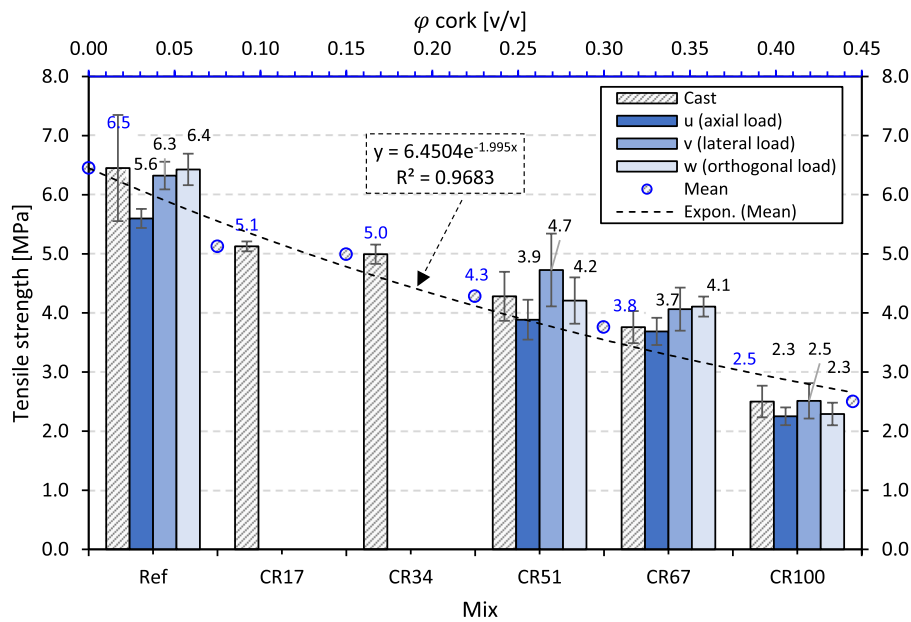**Fig. 26.** Variation in flexural strength with increase in volume content of cork in cast and printed specimens.

Fig. 27. Variation in tensile strength with increase in volume content of cork in cast and printed specimens.

Fig. 28. Fracture pattern of print samples tested in u direction for splitting tensile stress. (a) Reference mix; (b) CR51 mix; (c) CR67 mix; (d) CR100 mix.

demonstrates that lightweight and more sustainable mortars for 3D printing are a viable alternative to standard cement mortars with suitable mechanical strength and improved thermal insulation capacity.

This study focused on the mix design and fundamental material properties to verify the feasibility and advantages of introducing cork in printable mortars. It would be interesting that future works investigate
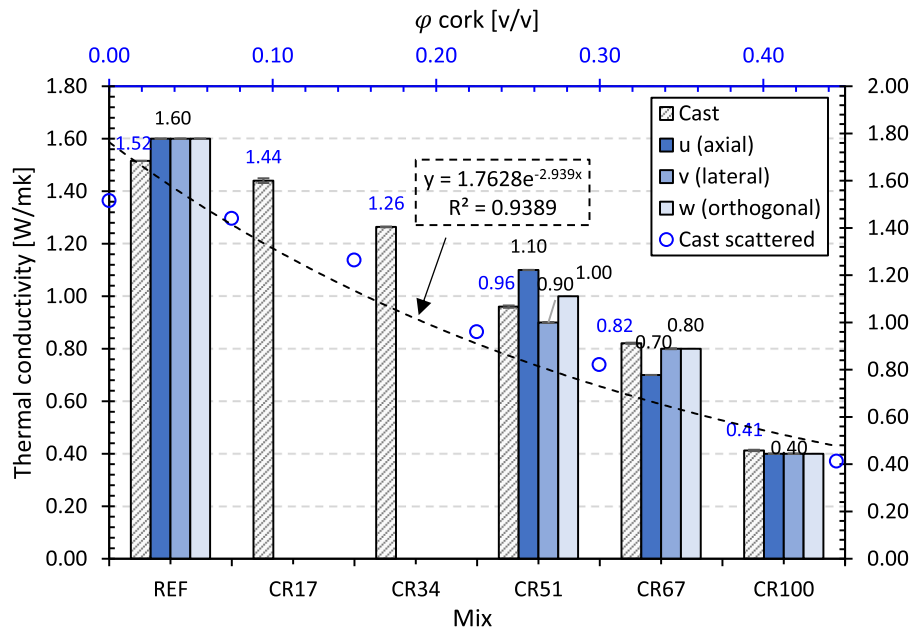
Fig. 29. Decrease in thermal conductivity of print and cast samples with increasing cork content.

durability aspects such as shrinkage and other parameters related to the extent of internal curing promoted by pre-soaked cork granules. In terms of large-scale applications, this study's findings suggest that the proposed compositions are compatible with 3D printing walls as load-bearing elements for low-strength load cases (i.e., low-rise buildings).

CRediT authorship contribution statement

C.M. Rangel: Writing – original draft, Methodology, Investigation, Formal analysis, Conceptualization, Data curation. **A.S. Guimarães:** Writing – review & editing, Supervision. **T.A.M. Salet:** Supervision, Writing – review & editing. **S.S. Lucas:** Writing – review & editing, Supervision.

Declaration of Competing Interest

The authors declare that they have no known competing financial interests or personal relationships that could have appeared to influence the work reported in this paper.

Data Availability

Data will be made available on request.

References

[1] International Energy Agency - Tracking Buildings *2022*. [Online] Available: ⟨https://www.iea.org/energy-system/buildings⟩.

[2] United Nations Environment Programme, *2022* Global Status Report for Buildings and Construction: Towards a Zero-emission, Efficient and Resilient Buildings and Construction Sector. [Online] Available: ⟨www.globalabc.org⟩.

[3] ACI Committee 213, ACI 213R-03 Guide for Structural Lightweight-Aggregate Concrete, American Concrete Institute, September 26, 2003 2003.

[4] M. Elshahawi, A. Hückler, M. Schlaich, Infra lightweight concrete: a decade of investigation (a review), Struct. Concr. vol. 22 (S1) (2020), https://doi.org/10.1002/suco.202000206.

[5] H.G. Şahin, A. Mardani-Aghabaglou, Assessment of materials, design parameters and some properties of 3D printing concrete mixtures; a state-of-the-art review, Constr. Build. Mater. vol. 316 (2022), https://doi.org/10.1016/j.conbuildmat.2021.125865.

[6] S. Ramakrishnan, S. Muthukrishnan, J. Sanjayan, K. Pasupathy, Concrete 3D printing of lightweight elements using hollow-core extrusion of filaments, Cem. Concr. Compos. vol. 123 (2021), https://doi.org/10.1016/j.cemconcomp.2021.104220.

[7] S. Pessoa, A.S. Guimarães, S.S. Lucas, N. Simões, 3D printing in the construction industry - A systematic review of the thermal performance in buildings, Renew. Sustain. Energy Rev. vol. 141 (2021), https://doi.org/10.1016/j.rser.2021.110794.

[8] "CONPrint3D® Ultralight - Production of monolithic, load-bearing wall constructions with very high thermal insulation through formwork-free deposition of foam concrete.".

[9] H. Marais, H. Christen, S. Cho, W. De Villiers, G. Van Zijl, Computational assessment of thermal performance of 3D printed concrete wall structures with cavities, J. Build. Eng. vol. 41 (2021), https://doi.org/10.1016/j.jobe.2021.102431.

[10] J. Sun, J. Xiao, Z. Li, X. Feng, Experimental study on the thermal performance of a 3D printed concrete prototype building, Energy Build. vol. 241 (2021), https://doi.org/10.1016/j.enbuild.2021.110965.

[11] M. Mohammad, E. Masad, T. Seers, S.G. Al-Ghamdi, High-Performance Light-Weight Concrete for 3D Printing, 2020//, in: F.P. Bos, S.S. Lucas, R.J.M. Wolfs, T.A.M. Salet (Eds.), Second RILEM International Conference on Concrete and Digital Fabrication, Springer International Publishing, Cham, 2020, pp. 459–467, 2020//.

[12] K. Cuevas, M. Chougan, F. Martin, S.H. Ghaffar, D. Stephan, P. Sikora, 3D printable lightweight cementitious composites with incorporated waste glass aggregates and expanded microspheres – Rheological, thermal and mechanical properties, J. Build. Eng. vol. 44 (2021), https://doi.org/10.1016/j.jobe.2021.102718.

[13] A. Bala, S. Gupta, Thermal resistivity, sound absorption and vibration damping of concrete composite doped with waste tire Rubber: A review, Constr. Build. Mater. vol. 299 (2021), https://doi.org/10.1016/j.conbuildmat.2021.123939.

[14] M. Sambucci, M. Valente, Influence of Waste Tire Rubber Particles Size on the Microstructural, Mechanical, and Acoustic Insulation Properties of 3D-Printable Cement Mortars, Civ. Eng. J. vol. 7 (6) (2021) 937–952, https://doi.org/10.28991/cej-2021-03091701.

[15] A.C. Composites. "Negative Carbon Balance." ⟨https://amorimcorkcomposites.com/en-us/why-cork/sustainability/⟩ (accessed 05 April 2023).

[16] A.K. Tedjditi, F. Ghomari, O. Taleb, R. Belarbi, R. Tarik Bouhraoua, Potential of using virgin cork as aggregates in development of new lightweight concrete, Constr. Build. Mater. vol. 265 (2020), https://doi.org/10.1016/j.conbuildmat.2020.120734.

[17] Y. Liu, Z. Cao, Y. Wang, D. Wang, J. Liu, Experimental study of hygro-thermal characteristics of novel cement-cork mortars, Constr. Build. Mater. vol. 271 (2021), https://doi.org/10.1016/j.conbuildmat.2020.121901.

[18] A.K. Tedjditi, F. Ghomari, R. Belarbi, R. Cherif, F. Boukhelf, R.T. Bouhraoua, Towards understanding cork concrete behaviour: Impact of considering cork

absorption during mixing process, Constr. Build. Mater. vol. 317 (2022), https://doi.org/10.1016/j.conbuildmat.2021.125905.

[19] D. Barnat-Hunek, R. Siddique, G. Łagód, Properties of hydrophobised lightweight mortars with expanded cork, Constr. Build. Mater. vol. 155 (2017) 15–25, https://doi.org/10.1016/j.conbuildmat.2017.08.052.

[20] A. Brás, M. Leal, P. Faria, Cement-cork mortars for thermal bridges correction. Comparison with cement-EPS mortars performance, Constr. Build. Mater. vol. 49 (2013) 315–327, https://doi.org/10.1016/j.conbuildmat.2013.08.006.

[21] M.G. Gomes, I. Flores-Colen, H. Melo, A. Soares, Physical performance of industrial and EPS and cork experimental thermal insulation renders, Constr. Build. Mater. vol. 198 (2019) 786–795, https://doi.org/10.1016/j.conbuildmat.2018.11.151.

[22] S. Merabti, S. Kenai, R. Belarbi, J. Khatib, Thermo-mechanical and physical properties of waste granular cork composite with slag cement, Constr. Build. Mater. vol. 272 (2021), https://doi.org/10.1016/j.conbuildmat.2020.121923.

[23] F. Craveiro, H.M. Bartolo, A. Gale, J.P. Duarte, P.J. Bartolo, A design tool for resource-efficient fabrication of 3d-graded structural building components using additive manufacturing, Autom. Constr. vol. 82 (2017) 75–83, https://doi.org/10.1016/j.autcon.2017.05.006.

[24] F. Craveiro, S. Nazarian, H. Bartolo, P.J. Bartolo, J. Pinto Duarte, An automated system for 3D printing functionally graded concrete-based materials, Addit. Manuf. vol. 33 (2020), https://doi.org/10.1016/j.addma.2020.101146.

[25] J. Chanut, et al., Surface properties of cork: Is cork a hydrophobic material? J. Colloid Interface Sci. vol. 608 (Pt 1) (Feb 15 2022) 416–423, https://doi.org/10.1016/j.jcis.2021.09.140.

[26] L.J. Gibson, K.E. Easterling, M.F. Ashby, Structure and mechanics of cork, Proc. R. Soc. (A377) (1981) 99–117.

[27] BS EN 196-1:2005 Methods of testing cement — Part 1: Determination of strength, 2005.

[28] EN 196-6 Methods of testing cement Part 6 Determination of fineness, 2010.

[29] EN 196-2:2013 Method of testing cement - Part 2: Chemical analysis of cement, 2013.

[30] R. Flatt, I. Schober, Superplasticizers and the rheology of concrete, *Underst. Rheol. Concr.* (2012) 144–208.

[31] M. Choi, N. Roussel, Y. Kim, J. Kim, Lubrication layer properties during concrete pumping, Cem. Concr. Res. vol. 45 (2013) 69–78, https://doi.org/10.1016/j.cemconres.2012.11.001.

[32] S. Hou, Z. Duan, J. Xiao, J. Ye, A review of 3D printed concrete: Performance requirements, testing measurements and mix design, Constr. Build. Mater. vol. 273 (2021), https://doi.org/10.1016/j.conbuildmat.2020.121745.

[33] NP EN 1097-6-2016 Tests for mechanical and physical properties of aggregates - Part 6_Determination of particle density and water absorption, 2016.

[34] D. Snoeck, C. Schröfl, V. Mechtcherine, Recommendation of RILEM TC 260-RSC: testing sorption by superabsorbent polymers (SAP) prior to implementation in cement-based materials, Mater. Struct. vol. 51 (5) (2018), https://doi.org/10.1617/s11527-018-1242-8.

[35] Test for mechanical and physical properties of aggregates - Part 3: Determination of loose bulk density and voids, 1998.

[36] EN 1015-3 -1999- A2 Methods of test for mortar for mansory - Part 3_Determination of consistence of fresh mortar (by flow table), 1999.

[37] EN 1015-6 Methods of test for mortar for mansory - Part 6_Determination of bulk density of fresh mortar, 1998.

[38] A.S.J. Suiker, R.J.M. Wolfs, S.M. Lucas, T.A.M. Salet, Elastic buckling and plastic collapse during 3D concrete printing, Cem. Concr. Res. vol. 135 (2020), https://doi.org/10.1016/j.cemconres.2020.106016.

[39] A. Tripathi, S.A.O. Nair, N. Neithalath, A comprehensive analysis of buildability of 3D-printed concrete and the use of bi-linear stress-strain criterion-based failure curves towards their prediction, Cem. Concr. Compos. vol. 128 (2022), https://doi.org/10.1016/j.cemconcomp.2022.104424.

[40] R.J.M. Wolfs, F.P. Bos, T.A.M. Salet, Early age mechanical behaviour of 3D printed concrete: numerical modelling and experimental testing, Cem. Concr. Res. vol. 106 (2018) 103–116, https://doi.org/10.1016/j.cemconres.2018.02.001.

[41] N. Roussel, Rheological requirements for printable concretes, Cem. Concr. Res. vol. 112 (2018) 76–85, https://doi.org/10.1016/j.cemconres.2018.04.005.

[42] T. Wangler, et al., Digital concrete: opportunities and challenges, RILEM Tech. Lett. vol. 1 (2016) 67–75, https://doi.org/10.21809/rilemtechlett.2016.16.

[43] EN 1015-10 Methods of test for mortar for mansory - Part 10 - Determination of dry bulk density of hardened mortar, 2006.

[44] EN 1015-11-1999-A1 Methods of test for mortar for mansory - Part 11-Determination of flexural and compressive strength of hardened mortar, 1999.

[45] EN 12390–6: 2009 Testing hardened concrete - Part 6: Tensile splitting strength of test specimens, 2009..

[46] ISO 8302:1991 Thermal insulation - Determination of steady-state thermal resistance and related properties - Guarded hot plate apparatus, 1991.

[47] Y.W.D. Tay, Y. Qian, M.J. Tan, Printability region for 3D concrete printing using slump and slump flow test, Compos. Part B: Eng. vol. 174 (2019), https://doi.org/10.1016/j.compositesb.2019.106968.

[48] P.K. Mehta, P.J.M. Monteiro, Microstructure of Concrete (ed). in Concrete: Microstructure, Properties, and Materials, Fourth ed., McGraw-Hill Education, New York, 2014.

[49] C.M. Rangel, A.S. Guimarães, T. Salet, and S.S.O. Lucas, Investigation of Admixtures and Water Uptake of Lightweight Aggregate Effect on the Rheological Behaviour of Mortar Mixes for 3D Printing, presented at the Concrete 2023, Perth, Australia, 2023. [Online]. Available: ⟨https://ciaconference.com.au/concrete 2023/content.html⟩.

[50] S. Muthukrishnan, S. Ramakrishnan, J. Sanjayan, Technologies for improving buildability in 3D concrete printing, Cem. Concr. Compos. vol. 122 (2021), https://doi.org/10.1016/j.cemconcomp.2021.104144.

[51] V.N. Nerella, M. Krause, V. Mechtcherine, Direct printing test for buildability of 3D-printable concrete considering economic viability, Autom. Constr. vol. 109 (2020), https://doi.org/10.1016/j.autcon.2019.102986.

[52] A.M. Solak, A.J. Tenza-Abril, V.E. Garcia-Vera, Influence of The Segregation Phenomenon on Structural Efficiency of Lightweight Aggregate Concretes, Mater. (Basel) vol. 13 (24) (Dec 16 2020), https://doi.org/10.3390/ma13245754.

[53] A.M. Neville, Properties of concrete, Pearson, Harlow, England; New York, 2011.

[54] R. Rodríguez-Álvaro, S. Seara-Paz, B. González-Fonteboa, V. Ferrándiz-Mas, K. Paine, Waste-Based porous materials as water reservoirs for the internal curing of Concrete. A review, Constr. Build. Mater. vol. 299 (2021), https://doi.org/10.1016/j.conbuildmat.2021.124244.

[55] A. Paul, S. Murgadas, J. Delpiano, P.A. Moreno-Casas, M. Walczak, M. Lopez, The role of moisture transport mechanisms on the performance of lightweight aggregates in internal curing, Constr. Build. Mater. vol. 268 (2021), https://doi.org/10.1016/j.conbuildmat.2020.121191.

[56] P. Trtik, , 2011, Release of internal curing water from lightweight aggregates in cement paste investigated by neutron and X-ray tomography, Nuclear Instruments and Methods in Physics Research Section A: Accelerators, Spectrometers, Detectors and Associated Equipment, vol. 651, no. 1, pp. 244-249, doi:10.1016/j.nima.2011.02.012.

[57] A. Borges, I. Flores-Colen, J. de Brito, Physical and mechanical performance of cement-based renders with different contents of fly ash, expanded cork granules and expanded clay, Constr. Build. Mater. vol. 191 (2018) 535–543, https://doi.org/10.1016/j.conbuildmat.2018.10.043.

[58] H. Xiong, K. Yuan, J. Xu, M. Wen, Pore structure, adsorption, and water absorption of expanded perlite mortar in external thermal insulation composite system during aging, Cem. Concr. Compos. vol. 116 (2021), https://doi.org/10.1016/j.cemconcomp.2020.103900.

[59] A. Gerritse, Design considerations for reinforced lightweight concrete, Int. J. Cem. Compos. Lightweight Concr. Volume 3 (Number 1) (1981).

[60] L.B. Satish Chandra, Noyes Publications, in: Lightweight aggregate concrete: science, technology, and applications, 1943, William Andrew Pub, Norwich, N.Y., 2022.

[61] C. Sergi, F. Sarasini, V. Fiore, E. Barbero, S. Sanchez-Saez, J. Tirillò, The effects of water absorption and salt fog exposure on agglomerated cork compressive response, Eur. J. Wood Wood Prod. vol. 80 (1) (2021) 101–114, https://doi.org/10.1007/s00107-021-01754-7.

[62] S. v h K. d Nederlanden, 501 Besluit van 13 december 2019, houdende wijziging van het Bouwbesluit 2012 en van enkele andere besluiten inzake bijna energie-neutrale nieuwbouw, 2019.